

## Article

# Comparative Study in Design of Fiber-Reinforced Concrete at Elevated Temperatures by Numerical Evaluation through Developed Hybrid Metaheuristic Algorithms

Lihua Chen <sup>1</sup>, Harry Far <sup>2,\*</sup>, Mina Mortazavi <sup>2</sup> and Adham E. Ragab <sup>3</sup> <sup>1</sup> Chongqing Vocational Institute of Engineering, Chongqing 402260, China; youtao@cmhk.com<sup>2</sup> School of Civil and Environmental Engineering, Faculty of Engineering and Information Technology, University of Technology Sydney (UTS), Ultimo, NSW 2007, Australia<sup>3</sup> Industrial Engineering Department, College of Engineering, King Saud University, P.O. Box 800, Riyadh 11421, Saudi Arabia

\* Correspondence: harry.far@uts.edu.au

**Abstract:** Fibrous concrete has good properties such as high ductility, high strength, suitable energy absorption and cracking resistance, which can be useful in many applications. This type of concrete is one of the best materials used in the construction of impact-resistant masonries, such as burial masonry structures, and explosive masonry warehouses. In this study, an artificial intelligence assessment based on the experimental test data from a laboratory has been performed on the fibrous concrete to evaluate the behavior of the samples at elevated temperatures and determine the most governing parameter on the mechanical properties of the fibrous concrete at elevated temperatures. For the first time, a hybrid intelligence algorithm has been developed based on the neural network structure using both genetic and swarm optimization algorithms. The ANFIS-PSO-GA (APG) algorithm was trained with experimental data and evaluated the flexural load and deflection of the samples. In order to detect the most prominent feature in the fire resistance of the fibrous concrete, five different subdatasets were designed. The results of the APG algorithm have been challenged with the ANFIS-PSO algorithm, which is a well-known hybrid numerical evaluation algorithm. As per the results, the newly designed APG algorithm has been successfully performed on both deflection and flexural prediction phases. Based on the numerical achievements, fiber features such as the fiber content and fiber mechanical properties are governing factors on the fibrous concrete resistance at elevated temperatures.

**Keywords:** prediction; artificial intelligence; ANFIS; mechanical properties; fiber; concrete



**Citation:** Chen, L.; Far, H.; Mortazavi, M.; Ragab, A.E. Comparative Study in Design of Fiber-Reinforced Concrete at Elevated Temperatures by Numerical Evaluation through Developed Hybrid Metaheuristic Algorithms. *Buildings* **2023**, *13*, 2045. <https://doi.org/10.3390/buildings13082045>

Academic Editors: Jijia Zhou and Chang Wu

Received: 1 June 2023

Revised: 29 July 2023

Accepted: 4 August 2023

Published: 10 August 2023



**Copyright:** © 2023 by the authors. Licensee MDPI, Basel, Switzerland. This article is an open access article distributed under the terms and conditions of the Creative Commons Attribution (CC BY) license (<https://creativecommons.org/licenses/by/4.0/>).

## 1. Introduction

Using reinforcing fibers, fibrous concrete (FC) in fact is a composite with higher tensile and compressive strength [1]. This composite has good integrity and consistency and enables concrete to be utilized as an appealing material for producing high-strength surfaces. FC is also extremely energy-absorbing and cannot be easily annihilated under impact loads. In the construction of industrial flooring, this type of concrete can be used instead of conventional reinforced concrete [2]. Other applications of this concrete include the construction of prefabricated building components such as canopy panels or concrete spraying on curved surfaces such as tunnels. Notably, concrete samples with moderate Al/Si ratios demonstrate greater resistance to structural evolutions compared to samples with other Al/Si ratios [3–5].

Applying this concrete to a structure also has the advantages of being insulated against sound and high-speed performance, but as the fibers inside the concrete are completely random, they cannot usually be used in concrete. Steel fibers resist crack propagation and increase concrete resistance against fatigue, impact, shrinkage and thermal stress. Polymeric

fibers used in concrete are natural and synthetic polymer and have various formulations, including acrylic, aramid, carbon, nylon, polyester, polyethylene (PE) and polypropylene (PP). Basalt fiber-reinforced polymer (BFRP) sheets significantly enhance the shear capacity and ductility of reinforced concrete (RC) beams, which has been demonstrated through experiments and validated with a cohesive element-based 3D finite-element model [6–9]. The uniform dispersion of fibers in cement-based materials enhances deformation performance, inhibits shrinkage, and improves fracture toughness [10–12]. Approximate costs and some of the leading mechanical and physical properties of polymeric fibers are indicated in Table 1 [13].

**Table 1.** Typical fiber features.

Fiber Type	Specific Gravity (kg/m <sup>3</sup> )	Modulus of Elasticity (Gpa)	Tensile Strength (Mpa)	Elongation at Break (%)	Acid/Alkali Resistance	Cost (\$/kg)
Polypropylene (PP) [14–16]	910	1.5–12	240–900	15–80	High	1–2.5
Polyethylene (PE) [17–19]	920–960	5–100	80–600	4–100	High	2–20
Steel (ST) for comparison [20]	7840	200	500–2000	0.5–3.5	Low to High	1–8

Concrete is a vulnerable material against fire and elevated temperatures; as per studies, spalling is the most significant shortcoming of plain concrete at elevated temperatures [21,22]. Likewise, other types of concrete against different heats may present complicated behavior like reducing compressive strength depending on the amount of exposure time and the level of the temperature. The strength at relatively low temperatures remains constant, and in some cases, it moderately increases. It is supposed that this increment is due to a hydration reaction between leftover unhydrated cement particles and the free water inside the concrete [23]. The strength reduces by about 15–40% when the temperature is close to 300 °C. At 550 °C, it decreases by about 55–70% compared to its initial value. The change in color is also seen in addition to the strength's change. Between 300 and 400 °C, the color changes from gray to red because of iron oxide oxidation, which is available in the aggregate and the cement paste. The compressive and flexural experiments performed by Lau and Anson were carried out on both plain concrete and 1% SFRC at elevated temperatures in the range of 105 °C and 1200 °C [24]. The authors reported that fibrous concrete with 0.25% to 0.5% of FC showed an average enhanced shear strength of 8.82% to 13.44% at higher temperatures up to 800 °C [25].

Based on a study of self-consolidating concrete containing PP fibers at elevated temperatures, a specific behavior was observed, which includes lower residual compressive strength than plain concrete. Accordingly, this performance was due to producing micro-channels along fibers melting at higher temperatures [26]. The elasticity modulus of concrete in subheated environments above 100 °C is approximately 100 times higher than that of PP samples, and it also increases about 1000 times at 150 °C [27]; in the volumes of 0.1% and 0.2%, the porosity of PPFRC increased considerably with rising temperature. At 300 °C, the relative porosity of PPFRC is 152% higher than that of non-fiber concrete. The splitting tensile, compressive strengths and elasticity modulus of PPFRC were reduced steadily with increasing temperature [28].

Raising the ambient state to 400 °C leads to improving the toughness of the PEFRC concrete which is due to the enhanced bond interactions induced by the increased molecular heat of the concrete texture and the fluxing surface of the PE fibers [29]. The behavior of mortar incorporating PP-PE fibers with a different dosage in the range of 0.3% to 1.2% subjected to elevated temperatures was evaluated, and it was found that the flexural deflection of this mortar has significantly increased compared to non-fiber specimens [30].

At 650 °C, the reduction in deflection of plain mortar was obtained by about 77%, while mortar containing 9% fiber was only about 13% (e.g., from 1.40 to 1.22 mm).

Although there are several investigations performed regarding FRC at elevated temperatures, most of the performed experiments were not able to indicate the capability of FRC. Frame beams offer easy construction, steel savings and robust seismic performance with optimized parameters [31–33]. For the identification of fiber properties, using a single value of mechanical strength at the first crack moment is not conservative. Likewise, based on the first crack strength, any conclusion could be misleading [34].

On the other hand, the flexural toughness test appears to be a more suitable option to reach the fiber's properties compared to the compression test. This is because the main purpose of mixing fibers into concrete is for enhancing the ability of concrete in terms of energy absorption and load bearing after the first crack [35–38]. Accordingly, by attributing the toughness indices to the related flexural toughness, reliable information would derive and empower better access to the properties of fiber under high temperatures [39]. The composite beam externally bonded with a carbon fiber-reinforced plastic plate enhances the flexural behavior and load capacity, providing a solution to weak tensile capacity in ordinary concrete beams [40]. By understanding the statistical random rules governing construction safety accidents, this research contributes to enhancing safety measures and risk management in the construction sector [41–43].

The partial inclusion of fiber in FRC leads to changes in the properties such as mechanical properties [44,45]. Although these changes could be seen in the experiment, realizing the most influencing parameter may not be easy at all. To solve this issue, employing artificial intelligence (AI) can be helpful [46–48]. On the one hand, an adaptive neuro-fuzzy inference system (ANFIS) automatically performs the learning and adaptation cycles, which is a compliment in comparison to other algorithms. On the other hand, ANFIS can process and evaluate multivariable problems without adjusted system factors just by employing simpler solutions [49]. The first priority of using ANFIS among other neural networks is avoiding a high nonlinearity of approaches. As a matter of fact, the ANFIS has been successfully used to find the most governing parameters of flexural strength [50]. Furthermore, ANFIS has the ability to diminish the ambiguity in the process by eliminating selected input parameters to prepare the most desirable prediction conditions [51]. In other words, the ANFIS network was used to convert the multiple performance characteristics into a single performance index. Establishing a database of 3D aggregates from X-ray CT scans enables realistic heterogeneous modeling and distributive analysis in concrete composite research [52]. Generally, fuzzy systems are used to interpret and assess the data; however, some shortcomings have already been faced with the use of these algorithms as accuracy and versatility. Particle swarm optimization (PSO) is an evolutionary intelligence algorithm that was inspired by the social behavior of bird flocking or fish schooling [53]. As per different studies, PSO is potentially comparable to genetic algorithm (GA), and it has been utilized satisfactorily in many engineering issues [54]. Due to the relatively irregular laboratory data in the concrete sector, as well as investigations on the application of different fibers, artificial intelligence models can be well suited for the prediction of FRC properties. This algorithm benefits from a swift convergence rate among the other evolutionary algorithms, and it is basically continuous. In this article, the optimization process is completed by the PSO algorithm. Since the objective function must be evaluated many times in metaheuristic algorithms, it is easier to use PSO instead of simulation software. Using a fuzzy neural network, we obtained the pattern between the variables of the problem and the objective function and then used it to calculate the bending load and concrete strength.

In order to identify FRC properties, for the first time, an ANFIS algorithm is adopted to work along with two different pioneer hybrid metaheuristic algorithms as PSO and PSO-GA not only to detect the most determining deflection factor of the FRC but also to predict the flexural response of the FRC at elevated temperatures. Based on an experimental test of FRC structural elements against higher-level heats, the inputs are collected and prepared for

the soft-computing section [55]. The APG algorithm is developed by laboratory data and employed to predict and evaluate the properties of the fibrous concrete. The ANFIS-PSO is performed to challenge the APG results. Based on the achieved results, the new APG algorithm was successfully developed where the behavior of the samples was accurately predicted, most of the governing factors for FRC design have been introduced, and the ways of a reliable design have been discussed.

## 2. Materials and Methods

### 2.1. Test Procedure and Data Derivation

The conducted data have been collected from a previous test that has worked on the same concept and characteristics [29]. All of the samples were produced from the same concrete in the 15 cm × 15 cm × 15 cm standard cubes. The method of curing for the concrete specimens involved a specific heating profile following the ISO 834 fire curve. The test specimens were subjected to a transient heating process in an electric furnace. Before heating, the specimens were covered with a layer of steel mesh to protect the furnace from potential damage caused by concrete debris resulting from explosive spalling. The objective of the mix design was to achieve a compressive strength of over 90 MPa and prevent explosive spalling under fire conditions. Figure 1 illustrated the oven chamber section based on ASTM E119-98. To better acknowledge the mix proportions, we have enlisted the significant properties below:

- Cement: ASIA@CEM I 52.5 N Portland cement was used to achieve high strength.
- Silica Fume: Grade 940 silica fume from Elkem Microsilica@ was included in the mix.
- Coarse Aggregate: Chippings with a maximum size of 10 mm were used as the coarse aggregate.
- Fine Aggregate: Natural river sands were used as the fine aggregate.
- Superplasticizer: Sika® Visc°Crete®-2192 (71800, Nilai, Negeri Sembilan D.K., Malaysia) was applied as a superplasticizer to improve workability.
- Polypropylene (PP) Fibers: Monofilament PP fibers, 12 mm long with a diameter of 30 µm, were included at a dosage of 0.2% in terms of volumetric content.
- Steel Fibers: Steel fibers with a length of 35 mm and a diameter of 540 µm, sourced from Dramix® 3D 6535BG (Bosfa ©, Manukau, Auckland, New Zealand), were used at a dosage of 1% in terms of volumetric content.



**Figure 1.** Specimens in oven chamber according to ASTM E119-98.

The mix design resulted in a slump of 170 mm, which was classified as S4 according to EN 12350-2, implying good workability.

In the case of the flexural load capacity test, for each sample, a simple support beam was used and three-point loading was applied to the 300 mm span with an identified rate of 0.05 in./min. In terms of the load–deflection curve, using a PC-based data acquisition system, the results were collected. The samples were subjected to three determined heats including 400 °C, 600 °C and 800 °C (Figure 2) [12]. As per Figure 3 according to

ASTM C1018, the toughness indices have been calculated by load–deflection curve derived from the test results. Temperatures increased according to the ASTM E119-98 standard temperature–time curve.

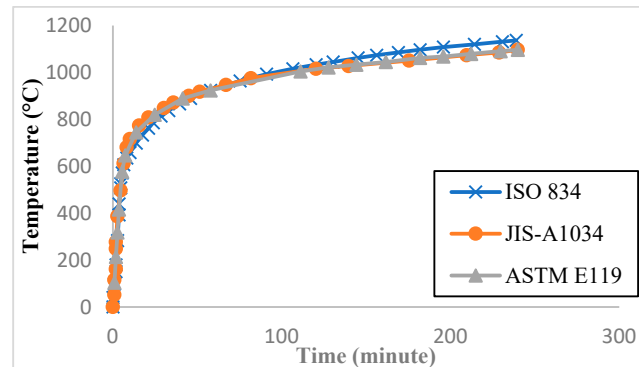


Figure 2. Standard fire curves.

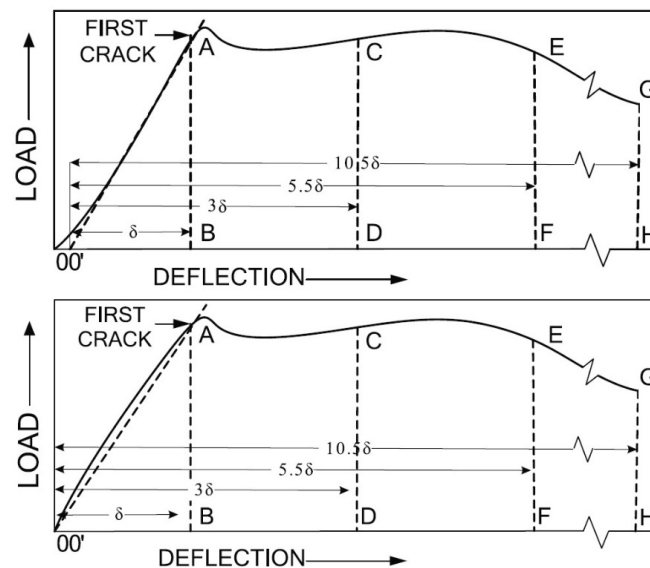


Figure 3. Process of calculating toughness indexes (ASTM C1018).

Prior to the peak, the FRC response was completely affected by the response of the concrete matrix. Whatever happened to plain concrete under high temperature showed similar effects on the pre-peak responses of the FRC. On the other hand, there are two factors that affect the post-peak flexural response of FRC including the temperature level and FRC type. At lower temperatures near 400 °C, the post-peak response was found to improve by a brief period of heat as seen by the increasing post-peak load and flexural toughness. By increasing the temperature to more than 400 °C, the type of fiber strongly affects the post-peak response. Due to the fiber evaporation, large drops of load–deflection responses were observed for the PP and PEFRC. As for the SFRC, heat leads to changing the color of the steel fiber but not evaporation; hence, high temperature does not affect the post-peak response of SFRC as much as it affects PP and PPFRC.

Here, the flexural characteristics are:

$$\text{Flexural toughness } (\delta) = \text{Area under the curve up to elastic limit (OAB)}$$

$$\text{Flexural index (I5)} = \text{Area OACD} / \text{Area OAB}$$

The flexural responses of different concrete schemes after exposure to high temperatures are given in Figures 4–7. At room temperature, the average peak load of plain concrete was 13 kN. The effect was not initiated immediately after exposure to high temperatures. The peak load stays unchanged at temperatures lower than 400 °C. At temperatures more than 400 °C, this effect was more noticeable: at 600 °C and 800 °C, it decreased by about 24% and 45%, respectively. In addition to strength, by increasing the temperature, the slope of the load–deflection curve decreased, which shows that the stiffness of the beam is also influenced by the temperature increment. Meanwhile, dramatic strength reduction could be attributed to the continuum cracking and spalling related to the thermal expansion inside composite elements.

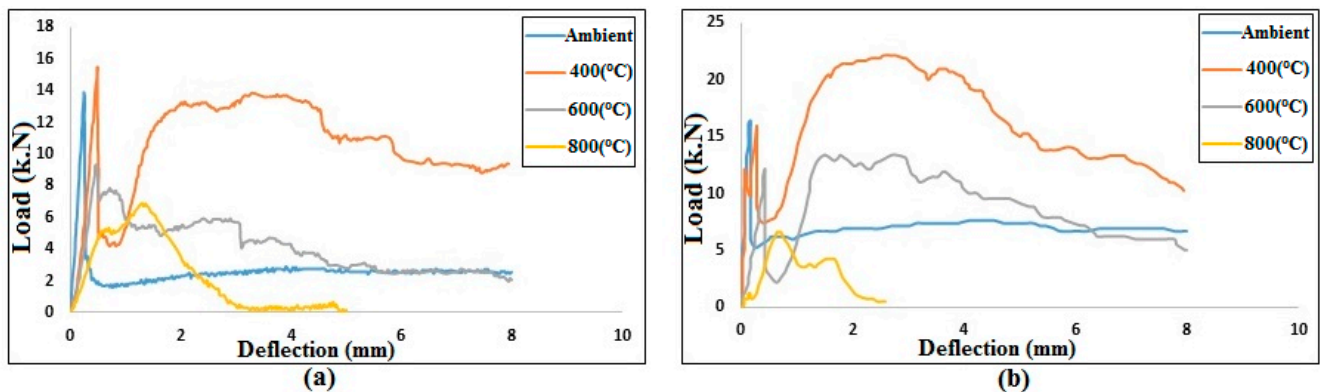


Figure 4. Flexural responses of (a) 0.5% PEFRC and (b) 1.0% PEFRC after thermal expansion.

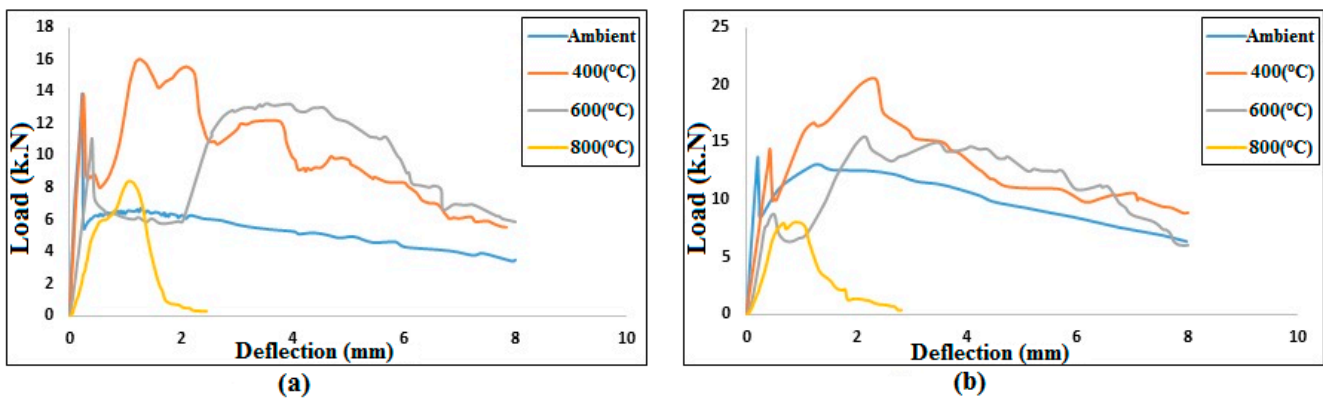


Figure 5. Flexural responses of (a) 0.5% PPFRC and (b) 1.0% PPFRC after thermal expansion.

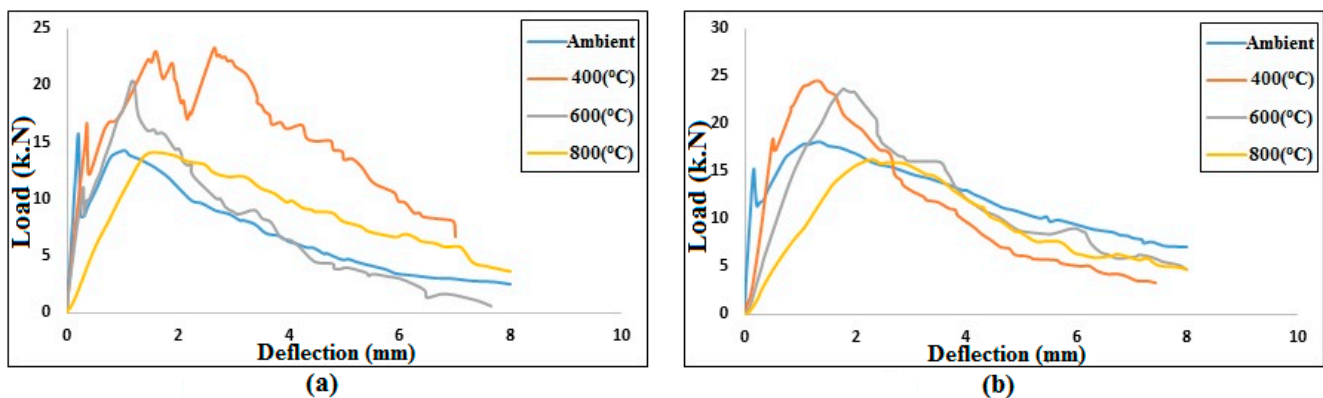


Figure 6. Flexural responses of (a) 0.5% SFRC and (b) 1.0% SFRC after thermal expansion.

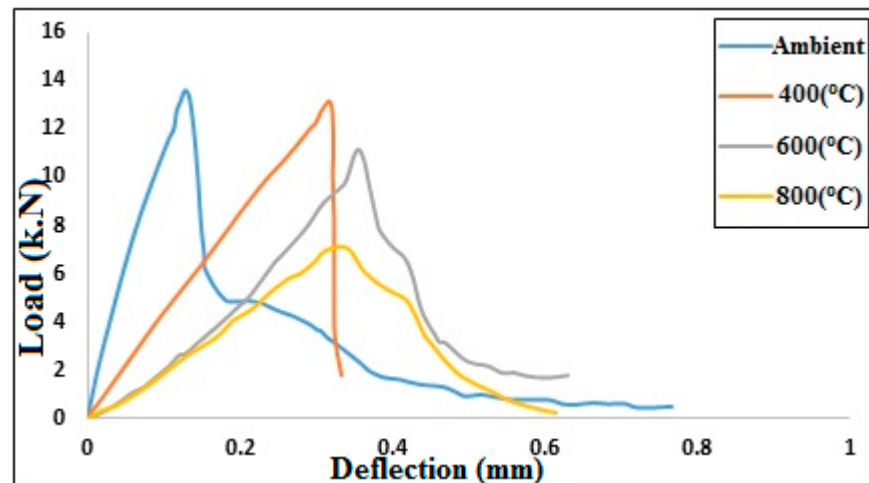


Figure 7. Flexural response of plain concrete after thermal expansion.

## 2.2. Artificial Intelligence Algorithms

### 2.2.1. ANFIS Architecture

ANFIS is a fuzzy inference system integrated within a neural network [50,56]. The ANFIS network has five layers (Figure 8) while the central core is a fuzzy inference system. The first layer receives inputs and converts them to fuzzy values by membership functions [57,58].

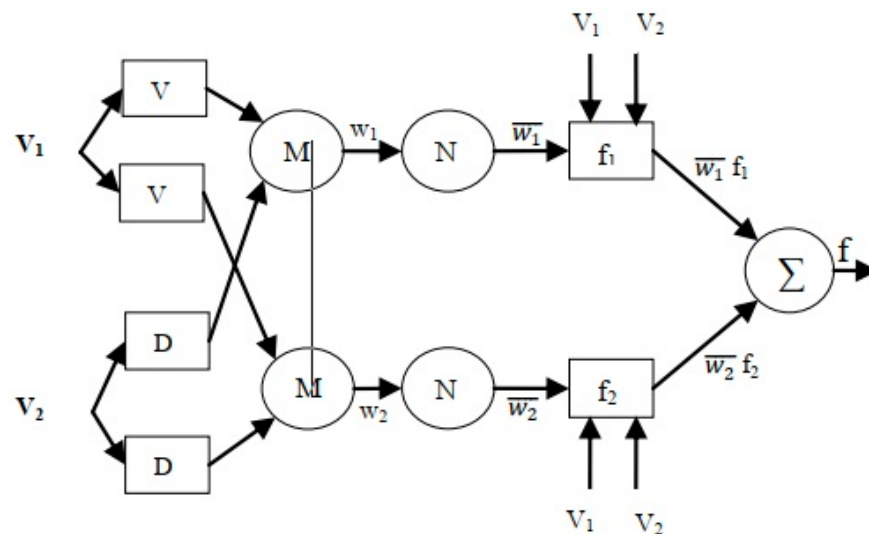


Figure 8. Typical architecture of ANFIS [2].

Based on the theory of ANFIS network abilities, a single node without any identified weight moves in a system of adjusted layers to another until the final node finds the correct answer [34,59,60]. The aforementioned cycle has been demonstrated in Figure 8; five layers are typically performed in succession and have a membership function effect on the final layer. Just in the case of conservation, the authors assume that the ANFIS has two described inputs such as  $V_1$  and  $V_2$ , and one output as  $f$ . According to the Takagi, Sugeno and Kang theory [34], two rules are described below:

First: Assuming ( $v$  is  $V_1$ ) and ( $d$  is  $D_1$ ), the output can be derived as  $f_1 = p_1v + q_1d + r_1$ .

Second: Assuming ( $v$  is  $V_2$ ) and ( $d$  is  $D_2$ ), the output can be derived as  $f_2 = p_2v + q_2d + r_2$ .

Here,

$p_1, p_2, q_1, q_2, r_1$  and  $r =$  linear parameters which are mostly adjusted and identified by training and testing procedures.

$V_1, V_2, D_1$  and  $D_2$  = nonlinear parameters, for instance  $V_1$  and  $D_1$  are the membership functions of ANFIS (antecedent).

It is clear that more accurate evaluation means a slight difference between the ANFIS answer and the real value [61,62].

First of all, an individual unweighted node moves in the first layer just by a node function, which has been represented as Equation (1).

$$O_i^1 = \mu A_i(x) \quad (1)$$

where

$A_i$  = linguistic label;

$O_i^1$  = membership function of  $A_i$ .

Accordingly, the bell-shaped function selects for adjustment in ANFIS while having the most capacity for nonlinear regression [55,63,64].

$$\mu(x) = bell(x; a_i, b_i, c_i) = \frac{1}{1 + \left[ \left( \frac{x-c_i}{a_i} \right)^2 \right]^{b_i}} \quad (2)$$

where

$\{a_i, b_i, c_i, d_i\}$  = adjusted factors;

$x$  = input.

The typical function of the second layer is described in Equation (3) while a node multiplies to the incoming signals and moves to the third layer.

$$w_i = \mu A_i(x) \times \mu B_i(y), \quad i = 1, 2. \quad (3)$$

The third layer is the rule layer. In fact, every output exhibits the firing strength of a rule.

$$w_i^* = \frac{w_i}{w_1 + w_2} \quad i = 1, 2. \quad (4)$$

where

$w_i^*$  = normalized firing strength;

As per the ANFIS rule, every input should turn into fuzzy mode, and the fourth layer has been designed to convert the nodes into defuzzied mode.

$$O_i^4 = w_i^* f_i = w_i^* (p_i x + q_i y + r_i) \quad (5)$$

where

$w_i^*$  = third layer output;

$\{p_i, q_i, r_i\}$  = adjusted factors.

In the final layer, the output of each cycle is derived as the evaluated value, which is computed by cumulating all the incoming signals.

$$O_1^5 = f = \sum_i w_i^* f_i \quad (6)$$

### 2.2.2. Particle Swarm Optimization

Kennedy and Eberhart have proposed an optimization algorithm based on the clustering and lifestyle of birds and fishes [65]. Generally, the first in PSO is the definition of an initial population and then searching for optima derived by recalculating generations without evolution operators such as crossover and mutation [21]. Particles are the potential solutions while moving along the solution space using their own experiences and reaching the optimum solutions. PSO is a powerful algorithm for optimization in nonlinear, non-convex and discontinuous environments. Using the PSO can solve all kinds of optimization problems, both continuous and discrete [53]. This algorithm is very strong

and efficient, but it needs to define much fewer parameters than other algorithms, and the development of this algorithm is actually very simple. It is better than other optimization methods. This algorithm has been widely used in optimization problems, and the goal of the PSO algorithm is to find the optimum of the objective function [51]. In this algorithm, the particles are the constituent units of our population and they cooperate with each other, and with their intelligence, a certain amount of intelligence is created that is not comparable to the intelligence of each of them. That is why it is called swarm intelligence [66]. The most important feature of each particle is its position, and the most important issue is what indicator or goal the particle suggests and at what speed it moves. In this paper, new positions of each point have been achieved through the adjusted velocity of the point which has been written in Equation (7). In other words, at every step, each particle is updated using the top two values as shown in Equation (8).

$$v(t+1) = v(t) + c_1 * rand(t) * (pbest(t) - position(t)) + c_2 * rand(t) * (gbest(t) - position(t)) \quad (7)$$

$$position(t+1) = position(t) + v(t+1) \quad (8)$$

where

$V(t+1)$  = upgrade velocity;

$P_{best}$  = best situation the particle has ever been able to reach;

$G_{best}$  = best position ever obtained by the particle population (collective intelligence).

Using the PSO algorithm, the calculation of the minimization of the objective function is performed. This algorithm selects the optimal state of the desired variables. In general, it may seem that multi-objective optimization algorithms should be used for this problem, but we will see in the following that these two objective functions are actually global points. It is optimized and therefore is enough to mean only one of them.

### 2.2.3. ANFIS-PSO Architecture

Figure 9 presents the diagram of the sequential PSO and ANFIS combination [66]. In each cycle of the hybrid system, the new velocity and particle can be presented by Equations (9) and (10):

$$v_i \rightarrow (t+1) = wv_i \rightarrow (t) + c_1\varnothing_1 \rightarrow .(p_i \rightarrow (t) - x_i \rightarrow (t)) + c_2\varnothing_2 \rightarrow .(p_i \rightarrow (t) - x_i \rightarrow (t)) \quad (9)$$

$$s_i \rightarrow (t+1) = s_i \rightarrow (t) + v_i \rightarrow (t+1) \quad (10)$$

where

$v_i \rightarrow$  = particles velocity;

$p_i \rightarrow$  = best point in the entire population;

$w$  = inertia weight;

$c_1$  and  $c_2$  = positive acceleration coefficients;

$\varnothing_1 \rightarrow$  and  $\varnothing_2 \rightarrow$  = random vectors;

$s_i \rightarrow$  = particles position.

Finally, according to  $v_i \rightarrow$  and  $s_i \rightarrow$ , the particle population tends to cluster around the best.

### 2.2.4. ANFIS-PSO-GA (APG) Architecture

Figure 10 shows the combination of sequential PSO-GA and ANFIS. In PSO, a swarm is initiated by a group of random resolutions as a particle; the whole concept has been represented in Equation (11), in which the new velocity could be provided.

$$v_i(t+1) = wv_i(t) + c_1\phi_1(p_i(t) - x_i(t)) + c_2\phi_2(p_i(t) - x_i(t)) \quad (11)$$

where

$c_1$  and  $c_2$  = positive acceleration coefficients;

$\vec{\phi}_1$  and  $\vec{\phi}_2$  = random vectors [0, 1];

$\vec{p}_{ig}$  = location of input point;  
 $W$  = inertia weight;

The new position for each point can be achieved by Equation (12).

$$s_i(t+1) = s_i(t) + v_i(t+1) \quad (12)$$

where

$\vec{s}_i$  = particle's position;

$\vec{v}_i$  = particle's velocity.

Based on  $\vec{v}_i$  and  $\vec{s}_i$ , the particle population tends to cluster around the best number.

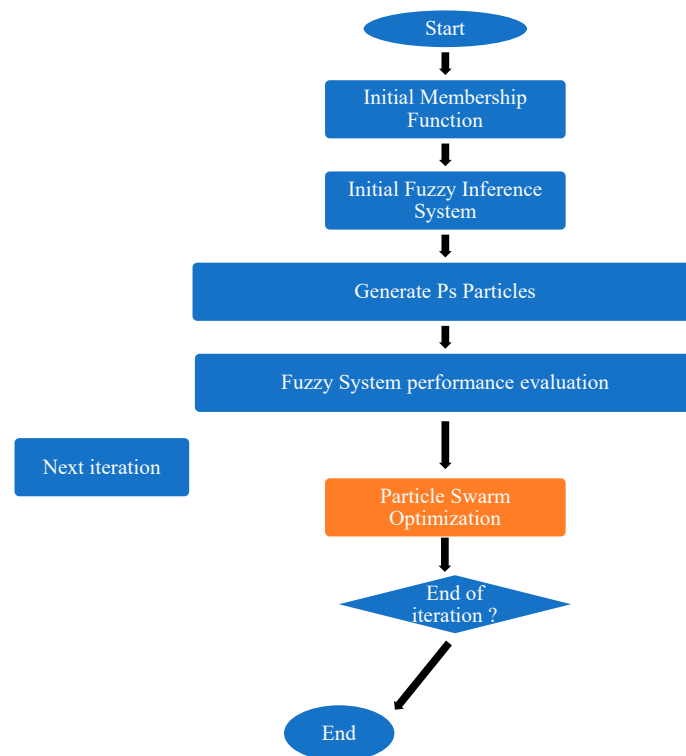


**Figure 9.** Diagram of the sequential combination of ANFIS-PSO algorithm.

### 2.3. Precision Evaluation

Accordingly, in the case of precision detection and performance evaluation, three well-known regression criteria were employed including the root mean squared error (RMSE), Pearson correlation coefficient ( $r$ ) and determination coefficient ( $R^2$ ) [67] as follows:

$$RMSE = \sqrt{\frac{\sum_{i=1}^n (P_i - O_i)^2}{n}} \quad (13)$$

$$r = \frac{n \left( \sum_{i=1}^n O_i \cdot P_i \right) - \left( \sum_{i=1}^n O_i \right) \cdot \left( \sum_{i=1}^n P_i \right)}{\sqrt{\left( n \sum_{i=1}^n O_i^2 - \left( \sum_{i=1}^n O_i \right)^2 \right) \cdot \left( n \sum_{i=1}^n P_i^2 - \left( \sum_{i=1}^n P_i \right)^2 \right)}} \quad (14)$$

$$R^2 = \frac{\left[ \sum_{i=1}^n (O_i - \bar{O}_i) \cdot (P_i - \bar{P}_i) \right]^2}{\sum_{i=1}^n (O_i - \bar{O}_i) \cdot \sum_{i=1}^n (P_i - \bar{P}_i)} \quad (15)$$

where  $P_i$  and  $O_i$  are the predicted and observed variables and  $n$  is the total number of considered data. Also, to compare the code performance of APG and ANFIS-PSO, MATLAB (2019) was deployed in one computer system with no external compiler or toolbox implementation.

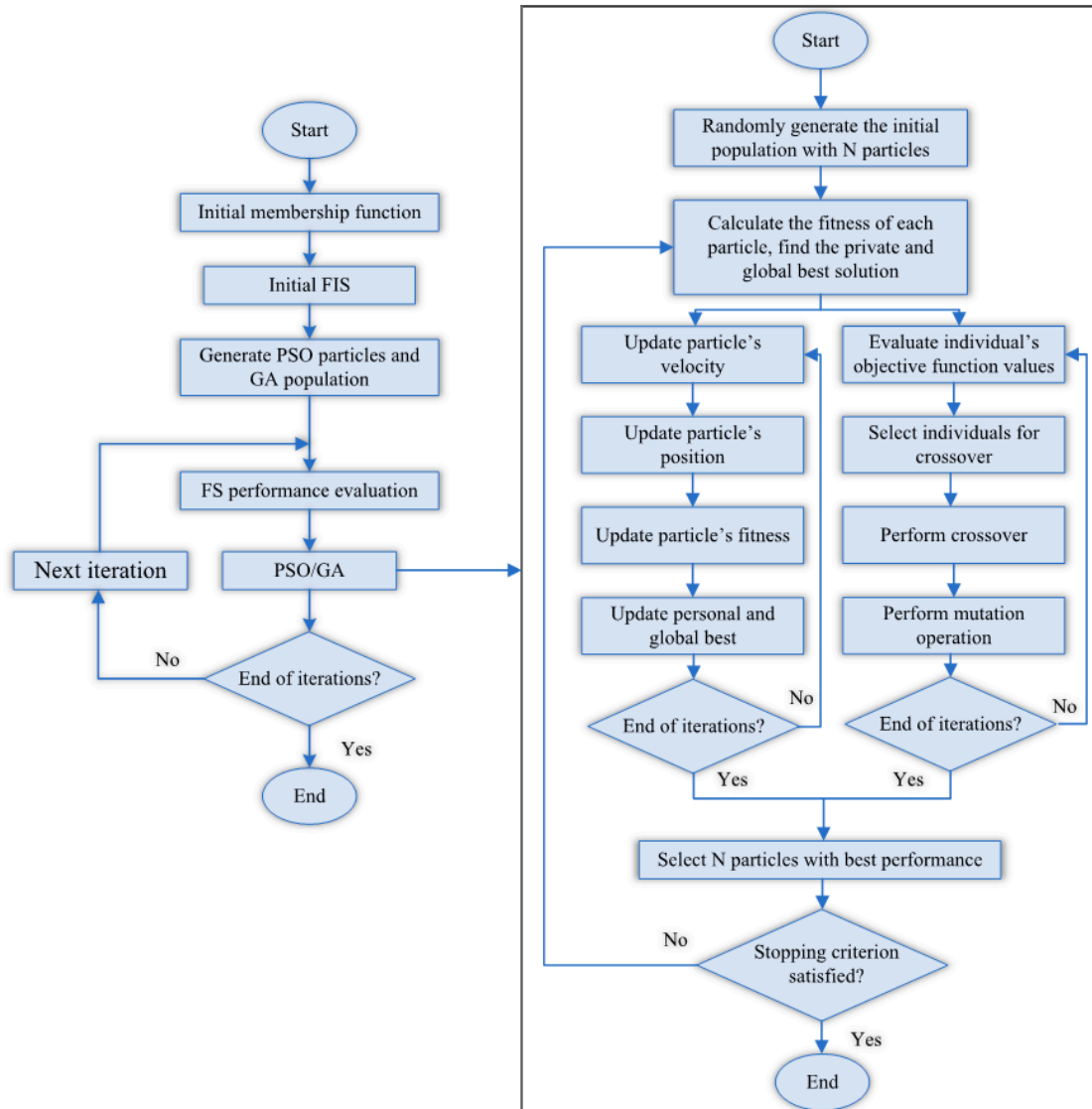


**Figure 10.** The sequential combination of hybrid APG algorithm.

#### 2.4. Statistical Data

To investigate and analyze the characteristics affecting the flexural response of the specimens exposed to high temperatures, we selected and studied nine structural parameters to more accurately predict the deflection and flexural capacity of the specimens [28]. The selected attributes are obtained based on the importance and quality of the experimental study in the preceding section. The collected database was composed of 2002 datasets. Experimental data of deflection ( $mm$ ), flexural capacity ( $k.N$ ), toughness index ( $\delta$ ), flexural index ( $I5$ ), pulse velocity ( $m/s$ ), fiber aspect ratio ( $l/d$ ), fiber content (%), fiber tensile strength ( $N/mm^2$ ) and temperature ( $^{\circ}C$ ) were used as inputs in each model for prediction and optimization. Table 2 shows the details of the dataset for hybrid models.

**Table 2.** Details of the input and output variables.

Inputs and Outputs	Variables	Minimum	Maximum	Mean Value	Standard Deviation
Input 1	Temperature ( $^{\circ}\text{C}$ )	25.00	800.00	456.25	272.92
Input 2	Fiber content (%)	0.00	1.00	0.50	0.23
Input 3	Tensile strength of fiber ( $\text{N./mm}^2$ )	450.00	1000.00	690.00	188.85
Input 4	Aspect ratio of fiber ( $l/d$ )	52.00	90.00	68.67	16.29
Input 5	Toughness index ( $I5$ )	1.80	6.80	3.91	1.42
Input 6	Flexural toughness ( $\delta$ )	1.10	12.50	2.54	1.95
Input 7	Pulse velocity ( $m/s$ )	2808	4795	4033.27	640.17
Input 8	Deflection ( $mm$ )	0.00	8.00	2.68	2.35
Input 9	Load ( $k.N$ )	0.00	24.54	7.29	5.29
Output 1	Load ( $k.N$ )	0.00	24.54	7.29	5.29
Output 2	Deflection ( $mm$ )	0.00	8.00	2.68	2.35
Output 3	Flexural toughness ( $\delta$ )	1.10	12.50	2.54	1.95

### 2.5. Models Development

As stated in the Section 1, the main purpose of this article is to find the most effective characteristic of fiber-reinforced concrete to optimize and predict the flexural response. In addition, with respect to the selected inputs and considering the different scenarios, the five subdatabases were chosen as the defining reference of these attributes [29], where subdatabase1 comprises mere flexural properties including ( $\delta$ ) and ( $I5$ ). Subdatabase2 focuses on the mere fiber properties, subdatabase3 only focuses on the pulse velocity characteristic and subdatabase4 and subdatabase5 both examined the flexural toughness. Thus, using each of these five subdatabases, one can analyze the effect of a key portion of FRC so that by comparing the results derived from their placement in artificial intelligence models, the quality of their effect and determination will be understood. A summary of this information can be found in Tables 3–7.

The provided paragraph discusses three variables: load, deflection, and temperature, which are present in three different subdatabases. Notably, the temperature variable is a pivotal attribute shared across all subdatabases because it serves as a reference point for the other variables, namely load and deflection. Moreover, within each subdatabase, the variables' load and deflection are interchangeable with one another, meaning they can act as either input or output, depending on their order of placement in the data structure. This flexibility in their roles within the subdatabases allows for different approaches in the analysis and interpretation of experimental results.

To ensure optimal performance and accuracy in the analyses, various metaheuristic parameters are employed. The process involves adjusting these parameters to achieve the best possible outcomes in terms of the stability and efficiency of the algorithms used for data processing and analysis. By fine-tuning these metaheuristic parameters, researchers can enhance the robustness of their algorithms and ensure reliable results during the data-driven exploration and investigation of the variables.

Overall, the following subdatasets outline the key elements of the research setup, including the importance of temperature as a pivotal attribute, the relationship between load, deflection, and the tea cloth properties, the interchangeability of load and deflection in the subdatabases, and the process of optimizing metaheuristic parameters to ensure algorithmic stability and reliability in the analysis of the gathered data.

**Table 3.** Inputs and outputs of subdatabase1.

Inputs and Outputs	Minimum	Maximum	Average
Temperature ( $^{\circ}\text{C}$ )	25.00	800.00	456.25
Flexural toughness ( $\delta$ )	1.10	12.50	2.54
Toughness index ( $I5$ )	1.80	6.80	3.91
Deflection ( $\text{mm}$ ) *	0.00	8.00	2.68
Load ( $\text{kN}$ ) *	0.00	24.54	7.29

\* Deflection and load were employed both as input and output.

**Table 4.** Inputs and outputs of subdatabase2.

Inputs and Outputs	Minimum	Maximum	Average
Temperature ( $^{\circ}\text{C}$ )	25.00	800.00	456.25
Fiber content (%)	0.00	1.00	0.50
Tensile strength of fiber ( $\text{N}/\text{mm}^2$ )	450.00	1000.00	690.00
Aspect ratio of fiber ( $l/d$ )	52.00	90.00	68.67
Deflection ( $\text{mm}$ ) *	0.00	8.00	2.68
Load ( $\text{kN}$ ) *	0.00	24.54	7.29

\* Deflection and load were employed both as input and output.

**Table 5.** Inputs and outputs of subdatabase3.

Inputs and Outputs	Minimum	Maximum	Average
Temperature ( $^{\circ}\text{C}$ )	25.00	800.00	456.25
Pulse velocity ( $\text{m}/\text{s}$ )	2808	4795	4033.27
Deflection ( $\text{mm}$ ) *	0.00	8.00	2.68
Load ( $\text{kN}$ ) *	0.00	24.54	7.29

\* Deflection and load were employed both as input and output.

**Table 6.** Inputs and outputs of subdatabase4.

Inputs and Outputs	Minimum	Maximum	Average
Temperature ( $^{\circ}\text{C}$ )	25.00	800.00	456.25
Fiber content (%)	0.00	1.00	0.50
Tensile strength of fiber ( $\text{N}/\text{mm}^2$ )	450.00	1000.00	690.00
Deflection ( $\text{mm}$ ) *	0.00	8.00	2.68
Flexural toughness ( $\delta$ ) *	1.10	12.50	2.54

\* Deflection and flexural toughness were employed both as input and output.

**Table 7.** Inputs and outputs of subdatabase5.

Inputs and Outputs	Minimum	Maximum	Average
Temperature ( $^{\circ}\text{C}$ )	25.00	800.00	456.25
Fiber content (%)	0.00	1.00	0.50
Tensile strength of fiber ( $\text{N}/\text{mm}^2$ )	450.00	1000.00	690.00
Load ( $\text{kN}$ )	0.00	24.54	7.29
Deflection ( $\text{mm}$ ) *	0.00	8.00	2.68
Flexural toughness ( $\delta$ ) *	1.10	12.50	2.54

\* Deflection and flexural toughness were employed both as input and output.

### 2.5.1. ANFIS-PSO Adjustment

Subdatabase1 was used as the base database to optimize the algorithm and find the best parameters for each artificial intelligence model. Accordingly, all parameters of the ANFIS-PSO hybrid algorithm were first considered constant, and only the population was adjusted so that by placing different population numbers, the first one was found to be better than the nearest population number that was optimized (Figure 11).

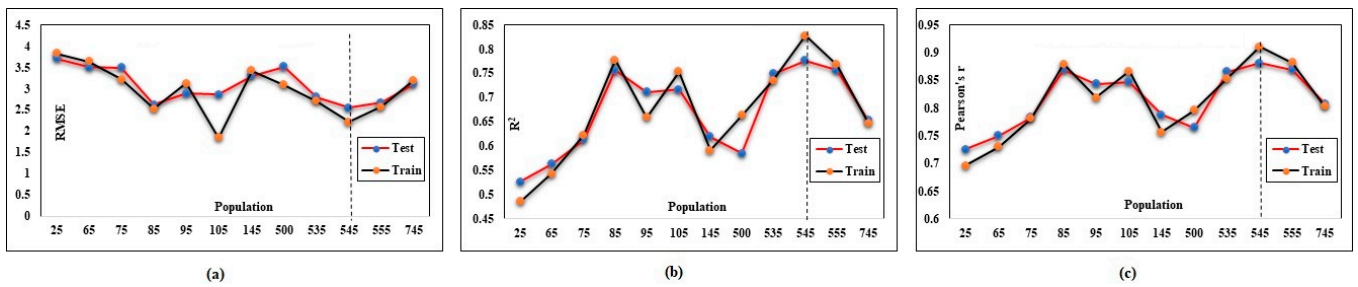


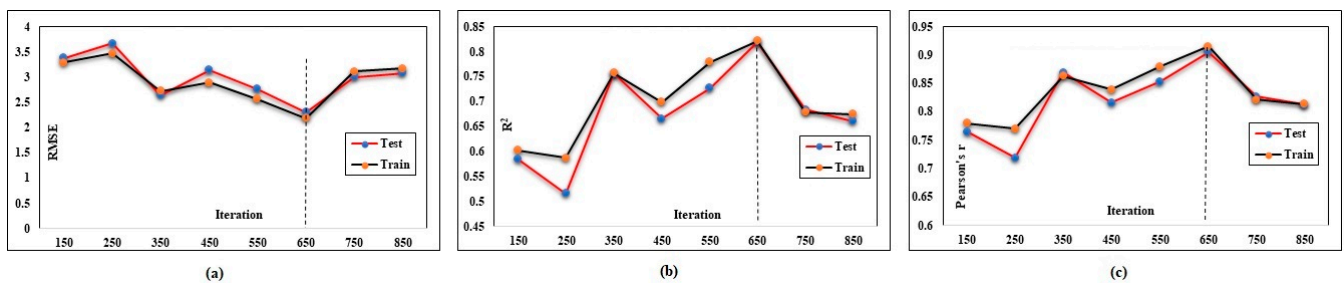
**Figure 11.** ANFIS-PSO adjustment based on population number: (a) effect of population number on (RMSE), (b) effect of population number on ( $R^2$ ), (c) effect of population number on ( $r$ ).

The obtained results were then documented and summarized in Table 8, which presents a comprehensive tabulation of the analytical performance parameters. These parameters likely include metrics related to accuracy, convergence, and efficiency, among others, that were used to assess and compare the performance of the different artificial intelligence models under consideration. By conducting this rigorous optimization process and recording the analytical performance parameters, the researchers were able to identify an optimal configuration for the ANFIS-PSO hybrid algorithm when applied to subdatabase1. This enhanced algorithm configuration likely contributed to more accurate and efficient analyses, potentially leading to improved results in various AI-based applications, such as pattern recognition, prediction, or decision-making tasks [66,67].

**Table 8.** Performance parameters of ANFIS-PSO adjustment based on population number.

Population	Test			Train		
	RMSE	$r$	$R^2$	RMSE	$r$	$R^2$
25	3.712577	0.725924	0.527	3.831084	0.696089	0.4859
65	3.508492	0.750727	0.5636	3.637986	0.729853	0.5429
75	3.497266	0.783102	0.6132	3.219799	0.781098	0.6227
85	2.626729	0.869537	0.7561	2.533611	0.879021	0.7777
95	2.885258	0.843709	0.7118	3.128901	0.818919	0.6597
105	2.865556	0.846867	0.7172	1.85006	0.866333	0.7532
145	3.30335	0.78746	0.6201	3.423689	0.756888	0.5915
500	3.513862	0.764782	0.5849	3.083961	0.796095	0.6635
535	2.803131	0.865807	0.7496	2.70398	0.853733	0.7355
545	2.55558	0.880936	0.776	2.223289	0.910195	0.828
555	2.669889	0.869614	0.7562	2.577172	0.881952	0.7678
745	3.110781	0.808255	0.6533	3.199169	0.803118	0.6475

The results presented in Table 8 reveal that the ANFIS-PSO algorithm achieved its optimal performance when configured with a population number of 545. Building upon this crucial finding, the subsequent step in the research investigation involved a more detailed exploration of the algorithm's behavior by adjusting the number of iterations as a variable (as depicted in Figure 12). The number of iterations plays a pivotal role in the convergence behavior of the algorithm and can significantly influence its overall performance. By systematically varying the number of iterations and monitoring its effects on the algorithm's convergence rate and accuracy, the researchers aimed to gain deeper insights into the algorithm's behavior and identify the most effective iteration count for achieving superior results.



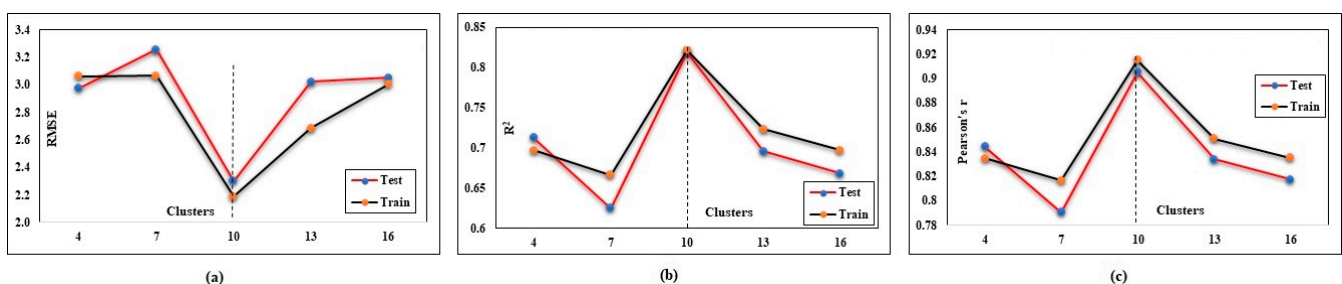
**Figure 12.** ANFIS-PSO adjustment based on iteration number: (a) effect of iteration number on (RMSE), (b) effect of iteration number on ( $R^2$ ), (c) effect of iteration number on ( $r$ ).

Figure 11 likely provides a graphical representation of the algorithm's performance across different iteration values, displaying trends such as convergence curves and convergence rates. Moreover, Table 9 presumably presents the test and train parameters used in the experimentation process. These parameters are crucial for evaluating the algorithm's generalization capabilities and its ability to perform accurately on unseen data (test set) after being trained on a known dataset (train set).

**Table 9.** Performance parameters of ANFIS-PSO adjustment based on iteration number.

Iteration	Test			Train		
	RMSE	$r$	$R^2$	RMSE	$r$	$R^2$
150	3.383412	0.764805	0.5849	3.292399	0.780195	0.6032
250	3.668915	0.718894	0.5168	3.463981	0.770327	0.5882
350	2.6410	0.869586	0.7562	2.7200	0.86274	0.7574
450	3.1374	0.81602	0.6659	2.8910	0.839018	0.6994
550	2.7653	0.852937	0.7275	2.5608	0.879944	0.7792
650	2.3018	0.905074	0.8192	2.1895	0.914906	0.8219
750	3.003843	0.826912	0.6838	3.1114	0.821586	0.6793
850	3.083801	0.812916	0.6608	3.171664	0.813298	0.6751

In the final phase, the cluster number parameter for the fuzzy segment was subjected to optimization. This parameter plays a significant role in fuzzy clustering algorithms, as it determines the number of clusters into which the data are partitioned. By visually examining the trends and patterns in Figure 13, it can gain insights into the algorithm's behavior as the cluster number changes and can identify the cluster number that leads to the most favorable outcomes in terms of cluster quality and separation. Furthermore, the specific results of this optimization process, along with corresponding performance metrics, are typically documented and tabulated in Table 10. This table offers a systematic overview of the algorithm's performance for each tested cluster number value.



**Figure 13.** ANFIS-PSO adjustment based on cluster number: (a) effect of cluster number on (RMSE), (b) effect of cluster number on ( $R^2$ ), (c) effect of cluster number on ( $r$ ).

**Table 10.** Performance parameters of ANFIS-PSO adjustment based on cluster number.

Clusters	Test			Train		
	RMSE	r	R <sup>2</sup>	RMSE	r	R <sup>2</sup>
4	2.9738	0.844155	0.7126	3.0613	0.834815	0.6969
7	3.2573	0.790532	0.6249	3.0672	0.816433	0.6666
10	2.3018	0.905074	0.8192	2.1895	0.914906	0.8219
13	3.0232	0.834038	0.6956	2.6844	0.850599	0.7235
16	3.0500	0.817362	0.6681	3.0039	0.834937	0.6971

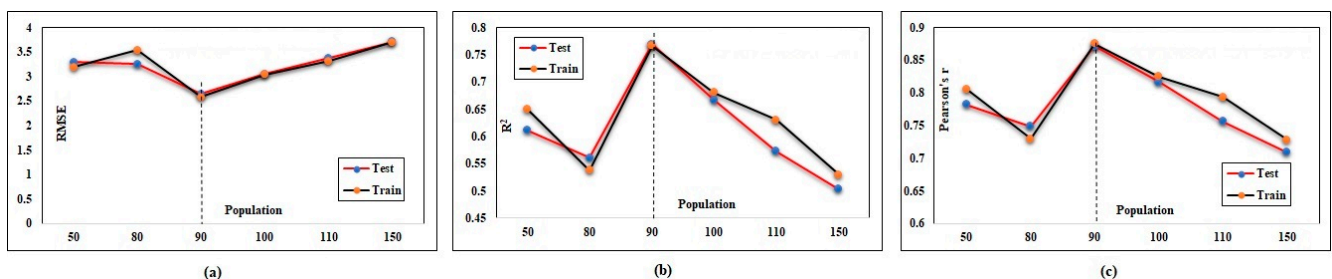
In this research study, the damping ratio parameter ( $w$ ) was a critical factor that underwent comprehensive investigation and fine-tuning. The damping ratio is a fundamental parameter in various optimization and control algorithms, and its adjustment plays a crucial role in determining the algorithm's stability and convergence characteristics. After a thorough evaluation, it was observed that the damping ratio value of 0.991 resulted in the best performance for the hybrid ANFIS-PSO program. This optimal value demonstrated superior convergence behavior, striking a balance between rapid convergence and preventing oscillations or divergence, thereby enhancing the algorithm's overall efficiency and effectiveness. To provide a clear and systematic presentation of the final parameter configuration, the researchers documented the results in Table 11. This table tabulates the optimized parameters, along with associated performance measures or other relevant metrics, providing a comprehensive overview of the hybrid ANFIS-PSO program's efficacy.

**Table 11.** Parameter characteristics utilized for ANFIS-PSO.

FIS Clusters	Population Size	Iterations	Inertia Weight	Damping Ratio	Learning Coefficient	
					Personal	Global
10	545	650	1.00	0.991	1	2

### 2.5.2. APG Adjustment

Accordingly, each step has been presented briefly, as the technical process was the same as in the previous section. In this section, subdatabase1 was used to adjust the different parameters of the ANFIS-PSO-GA algorithm, as was the case for the ANFIS-PSO algorithm. Initially, the algorithm efficiency was evaluated by changing the population number. As can be seen in Figure 14, a population of 90 yields the best algorithm returns. Table 12 lists the numerical accuracy indices corresponding to each imported population.

**Figure 14.** APG adjustment based on population number: (a) effect of population number on (RMSE), (b) effect of population number on (R<sup>2</sup>), (c) effect of population number on (r).

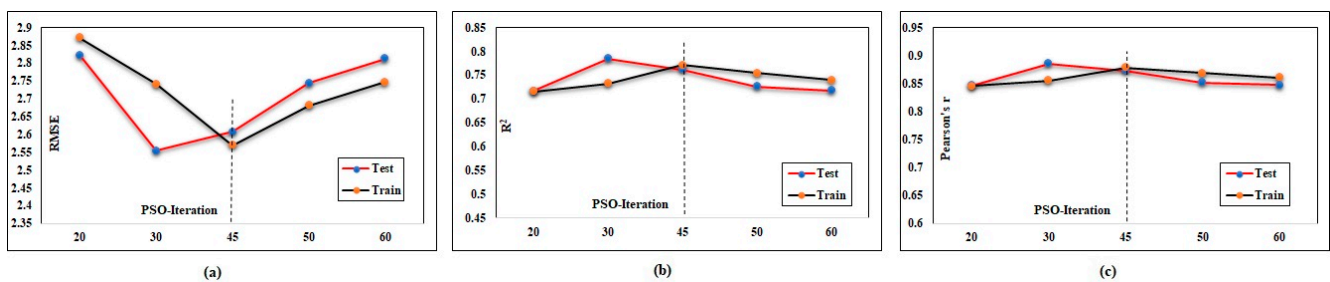
**Table 12.** Performance parameters of APG adjustment based on population number.

Population	Test			Train		
	RMSE	r	R <sup>2</sup>	RMSE	r	R <sup>2</sup>
50	3.299182	0.781941	0.6114	3.195194	0.806186	0.6499
80	3.255189	0.749049	0.5611	3.534075	0.729853	0.5382
90	2.643244	0.871738	0.7699	2.587535	0.875461	0.7664
100	3.054091	0.816756	0.6671	3.045109	0.825002	0.6806
110	3.376154	0.756638	0.5725	3.310291	0.793831	0.6302
150	3.716255	0.709193	0.503	3.696705	0.728039	0.53

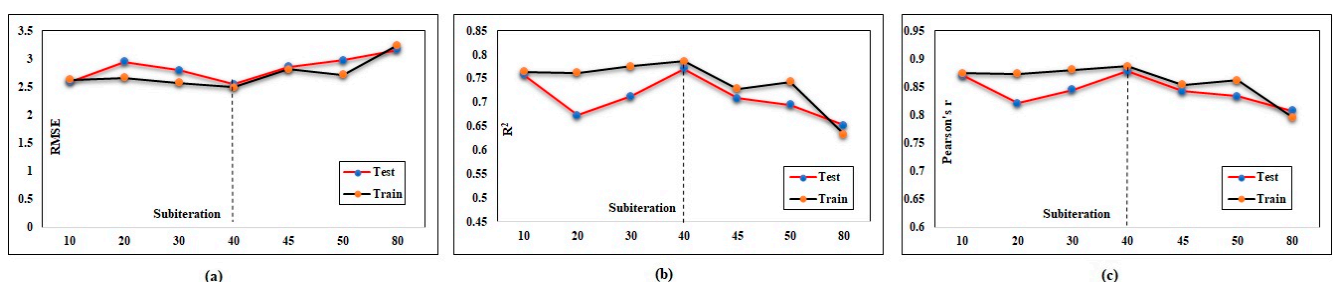
Further, considering a population of 90, using subdatabase1, another parameter of the PSO algorithm is adjusted. Different PSO iterations were tested, and the results are presented in Table 13 and Figure 15.

**Table 13.** Performance parameters of APG adjustment based on iteration number.

PSO Iteration	Test			Train		
	RMSE	r	R <sup>2</sup>	RMSE	r	R <sup>2</sup>
20	2.823024	0.846474	0.7165	2.871513	0.84599	0.7157
30	2.554562	0.886002	0.785	2.741211	0.855664	0.7322
45	2.607353	0.872721	0.7616	2.569105	0.878173	0.7712
50	2.744641	0.852209	0.7263	2.680724	0.868312	0.754
60	2.813234	0.84719	0.7177	2.74642	0.860313	0.7401

**Figure 15.** APG adjustment based on PSO iteration number: (a) effect of iteration number on (RMSE), (b) effect of iteration number on (R<sup>2</sup>), (c) effect of iteration number on (r).

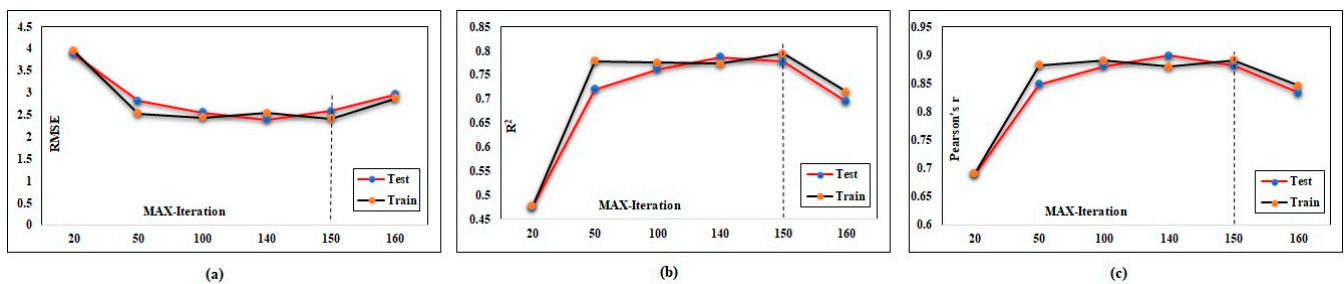
According to Table 13, the number of PSO iterations is considered to be 45. The number of sub-iterations was also adjusted as one of the adjustable parameters in the GA algorithm. As can be seen in Figure 16 and Table 14, the PSO-GA algorithm has shown its best numerical efficiency in sub-iteration number 40.

**Figure 16.** APG adjustment based on GA sub-iteration number: (a) effect of sub-iteration number on (RMSE), (b) effect of sub-iteration number on (R<sup>2</sup>), (c) effect of sub-iteration number on (r).

**Table 14.** Performance parameters of APG adjustment based on GA sub-iteration number.

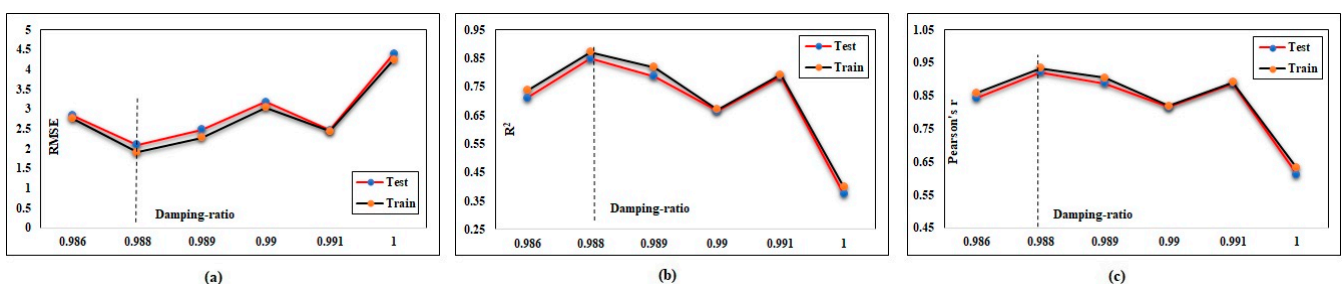
GA Sub-Iteration	Test			Train		
	RMSE	r	R <sup>2</sup>	RMSE	r	R <sup>2</sup>
10	2.590722	0.870225	0.7573	2.627477	0.873973	0.7638
20	2.942502	0.820655	0.6735	2.656337	0.873065	0.7622
30	2.795555	0.844398	0.713	2.570393	0.880338	0.775
40	2.548629	0.877919	0.7707	2.487351	0.886501	0.7859
45	2.858059	0.841623	0.7083	2.813826	0.85322	0.728
50	2.975344	0.833438	0.6946	2.712527	0.861689	0.7425
80	3.161902	0.807712	0.6524	3.241185	0.796085	0.6338

In the following, the MAX iteration is optimized as another parameter of the GA algorithm; the tuning process of the MAX iteration number is given in Figure 17 and Table 15.

**Figure 17.** APG adjustment based on MAX iteration number: (a) effect of MAX iteration number on (RMSE), (b) effect of MAX iteration number on (R<sup>2</sup>), (c) effect of MAX iteration number on (r).**Table 15.** Performance parameters of APG adjustment based on MAX iteration number.

Max Iteration	Test			Train		
	RMSE	r	R <sup>2</sup>	RMSE	r	R <sup>2</sup>
20	3.880335	0.690107	0.4762	3.943241	0.691182	0.4777
50	2.809624	0.848597	0.7201	2.533668	0.882422	0.7787
100	2.553774	0.880666	0.7618	2.441867	0.889812	0.7756
140	2.393413	0.898524	0.7873	2.538099	0.879129	0.7729
150	2.589503	0.881595	0.7772	2.411496	0.890905	0.7937
160	2.964227	0.833475	0.6947	2.866023	0.845298	0.7145

Finally, the damping ratio ( $w$ ) parameter was investigated and adjusted to obtain the most accurate results (Figure 18). According to Table 16, the most appropriate figure for  $w$  is 0.988, which yields the best numerical results.

**Figure 18.** APG adjustment based on damping ratio number: (a) effect of damping ratio number on (RMSE), (b) effect of damping ratio number on (R<sup>2</sup>), (c) effect of damping ratio number on (r).

**Table 16.** Performance parameters of APG adjustment based on damping ratio.

Damping Ratio	Test			Train		
	RMSE	r	R <sup>2</sup>	RMSE	r	R <sup>2</sup>
0.986	2.836168	0.843828	0.712	2.757289	0.859219	0.7383
0.988	2.104214	0.921673	0.8495	1.903745	0.934057	0.8725
0.989	2.477554	0.887488	0.7876	2.279348	0.905039	0.8191
0.99	3.17987	0.816025	0.6659	3.034619	0.81916	0.671
0.991	2.470995	0.887526	0.7877	2.444386	0.89027	0.7926
1.00	4.399623	0.611487	0.3739	4.249338	0.631111	0.3983

The derived performance parameters were tuned for the hybrid APG program and tabulated in Table 17.

**Table 17.** Parameter characteristics employed for APG.

FIS Clusters	Population Size	PSO Iterations	GA Sub-Iteration	MAX Iteration	Inertia Weight	Damping Ratio	Learning Coefficient	
							Personal	Global
10	90	50	45	150	1.00	0.988	1	2

### 3. Results and Discussion

#### 3.1. ANFIS-PSO

As explained in the previous section, the parameters of the ANFIS-PSO algorithm were adjusted according to Table 11. The process of analysis was initiated from subdatabase1 to subdatabase5 with the new optimized algorithm. Initially, the inputs of subdatabase1 were defined and predicted, and the flexural load and deflection were predicted separately through different analyses.

In this stage of the research, the obtained results were thoroughly analyzed and presented using regression graphs and comparative graphs, as depicted in Figures 19 and 20, respectively. Regression graphs are useful for visually assessing the relationship between predicted values and actual values, enabling researchers to evaluate the accuracy and reliability of the algorithm's predictions. On the other hand, comparative graphs allow for a side-by-side comparison of the predicted values with the ground truth data, offering insights into the algorithm's performance across different samples or experimental conditions. In conjunction with the graphical representations, Table 18 was utilized to present the detailed results of the analysis. This table likely contains quantitative metrics and statistical measures, such as root mean square error (RMSE), standard deviation (Std), or the coefficient of determination (R-squared), which are commonly used to assess the predictive performance of regression models. The results in Table 18 serve as a comprehensive reference for evaluating the algorithm's accuracy and precision in predicting both flexural strength and deflection values of the samples. According to the outcomes illustrated in Figure 20, the algorithm demonstrates the ability to predict the flexural strength and deflection of the samples with acceptable errors, which are denoted as "normal errors." This suggests that the algorithm performs reasonably well in capturing the underlying patterns and trends in the data, leading to predictions that are generally close to the actual values. However, it is important to note that the results are not precisely in line with the real values, indicating that there is still room for improvement in the predictive accuracy of the algorithm.

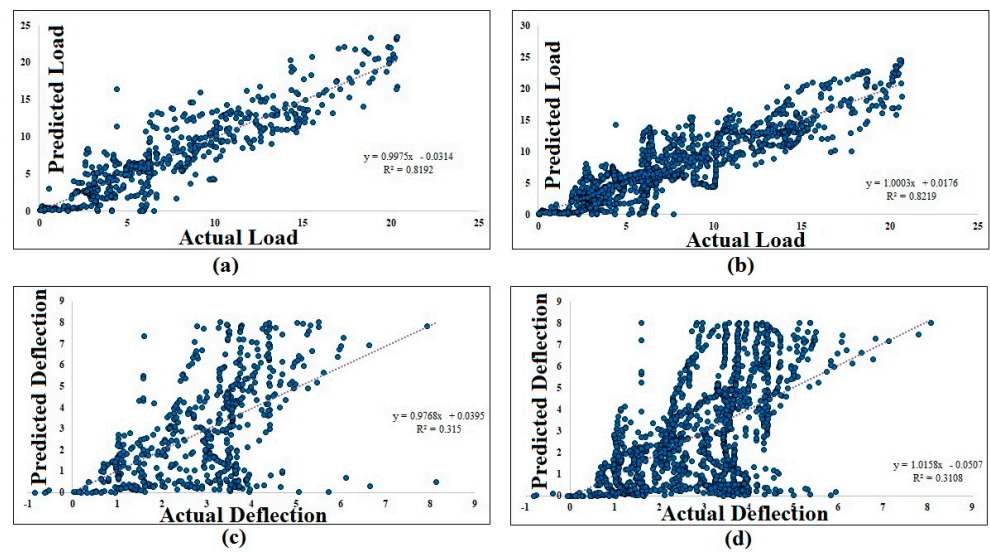


Figure 19. ANFIS-PSO prediction vs. experimental results regression for subdatabase1: (a) flexural load test phase, (b) flexural load train phase, (c) deflection test phase, (d) deflection train phase.

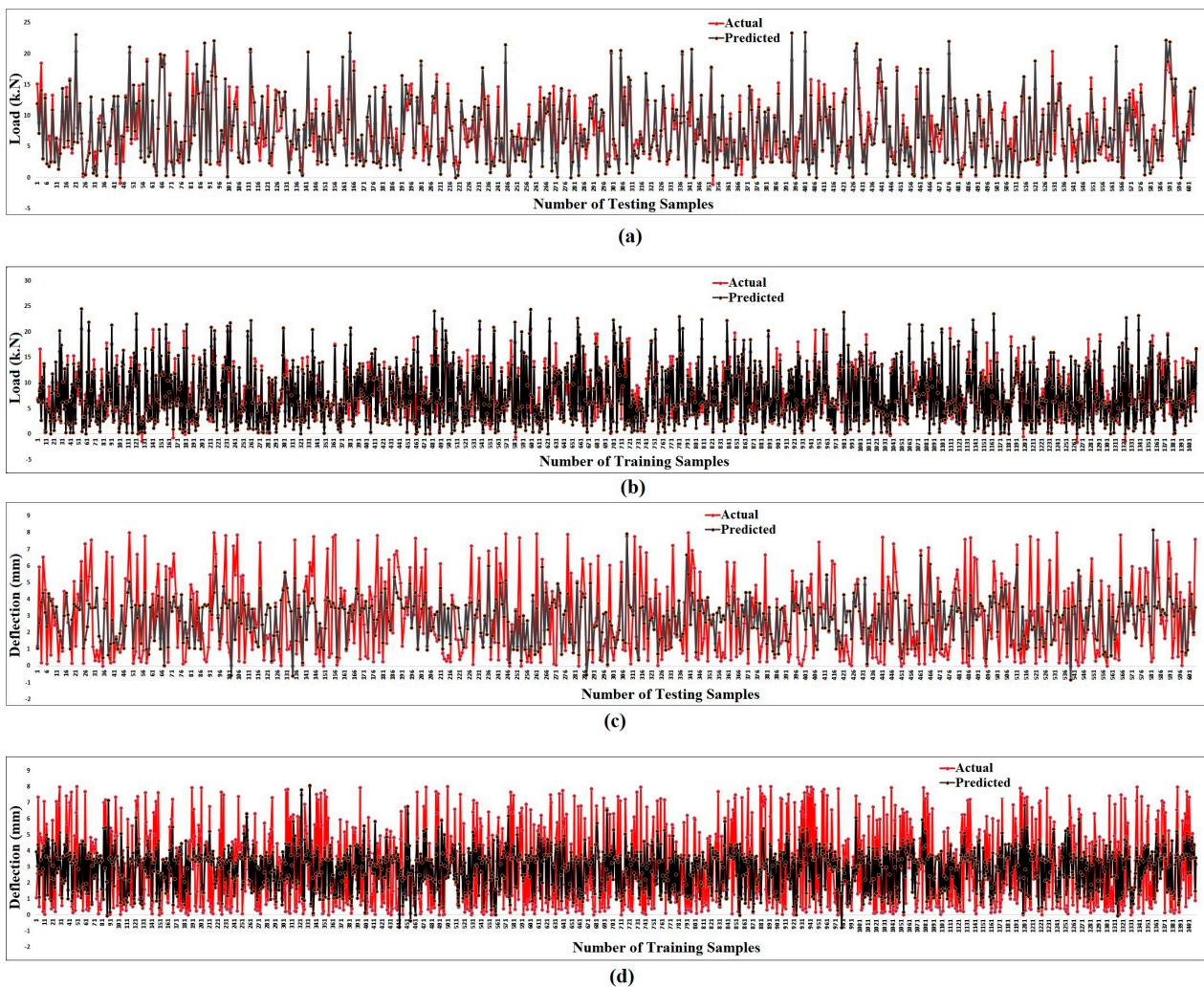


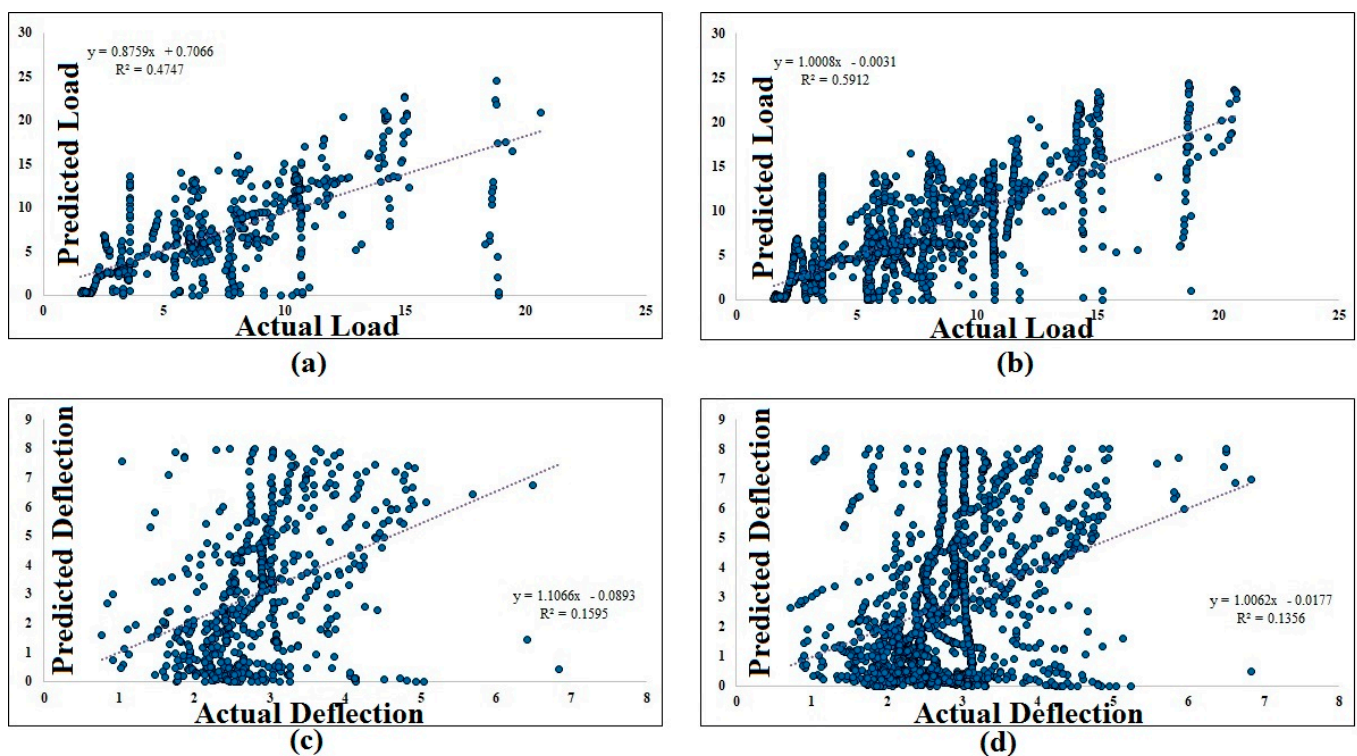
Figure 20. ANFIS-PSO prediction vs. experimental diagram for subdatabase1: (a) flexural load test phase, (b) flexural load train phase, (c) deflection test phase, (d) deflection train phase.

**Table 18.** Subdatabase1 analytical prediction results through ANFIS-PSO.

		Test		Train	
<b>Flexural load prediction</b>	RMSE	2.3018	RMSE	2.1895	
	R <sup>2</sup>	0.8192	R <sup>2</sup>	0.8219	
	r	0.9051	r	0.9149	
	Std *	2.3032	Std	2.2517	
	e mean	0.0502	e mean	0.0196	
		Test		Train	
<b>Deflection prediction</b>	RMSE	1.9248	RMSE	1.9257	
	R <sup>2</sup>	0.3150	R <sup>2</sup>	0.3108	
	r	0.5613	r	0.5514	
	Std	1.9262	Std	1.9394	
	e mean	0.0270	e mean	0.0048	

\* Std = standard deviation.

Then, using subdatabase2, the corresponding inputs are defined, and flexural load and deflection are estimated and predicted in two steps (Figures 21 and 22). Table 19 concluded the performance precision parameters of this phase. As the subdatabase1 results show, the ANFIS-PSO algorithm has estimated the mechanical properties of the samples with considerable convergence against the real values.

**Figure 21.** ANFIS-PSO prediction vs. experimental results regression for subdatabase2: (a) flexural load test phase, (b) flexural load train phase, (c) deflection test phase, (d) deflection train phase.

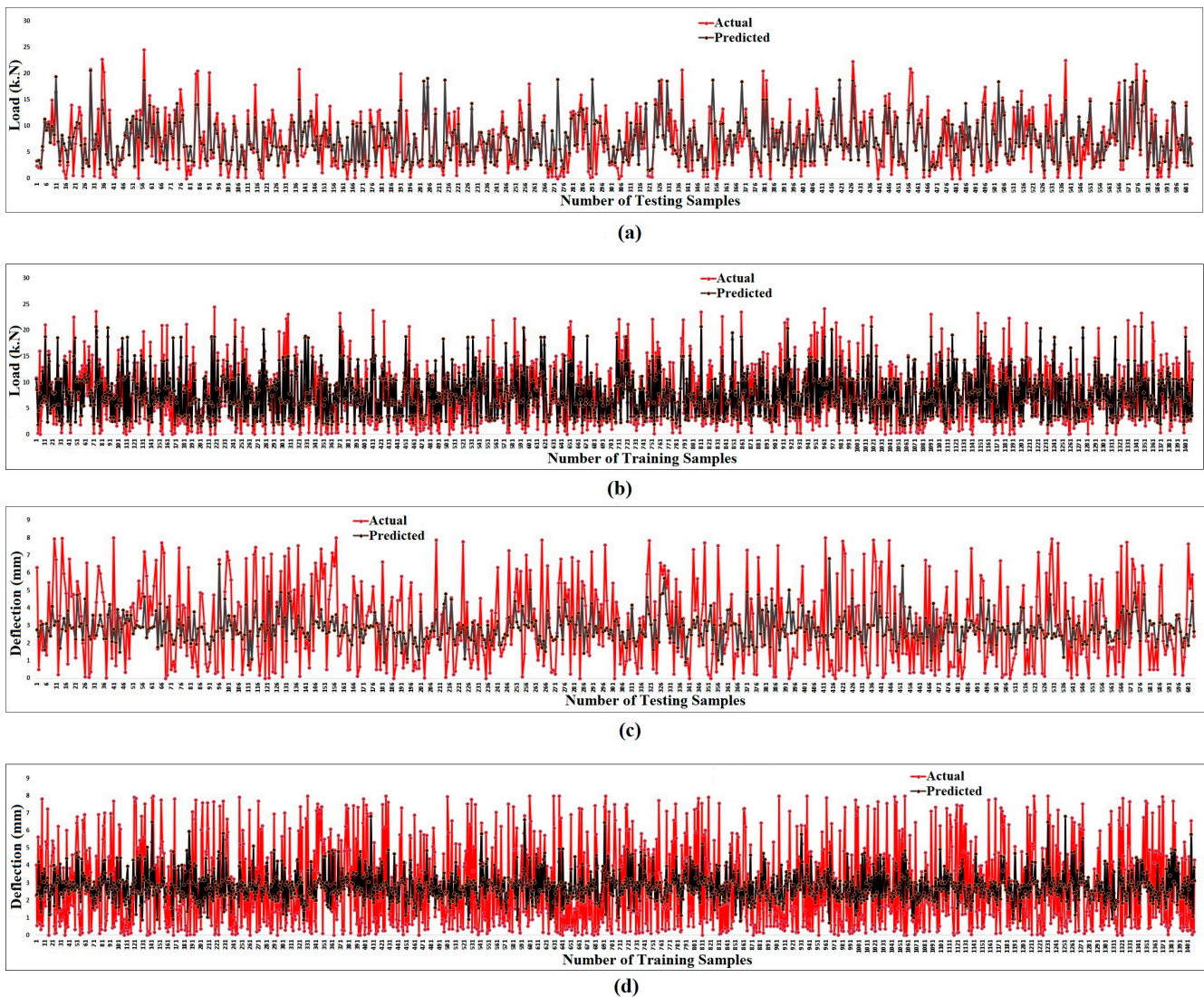


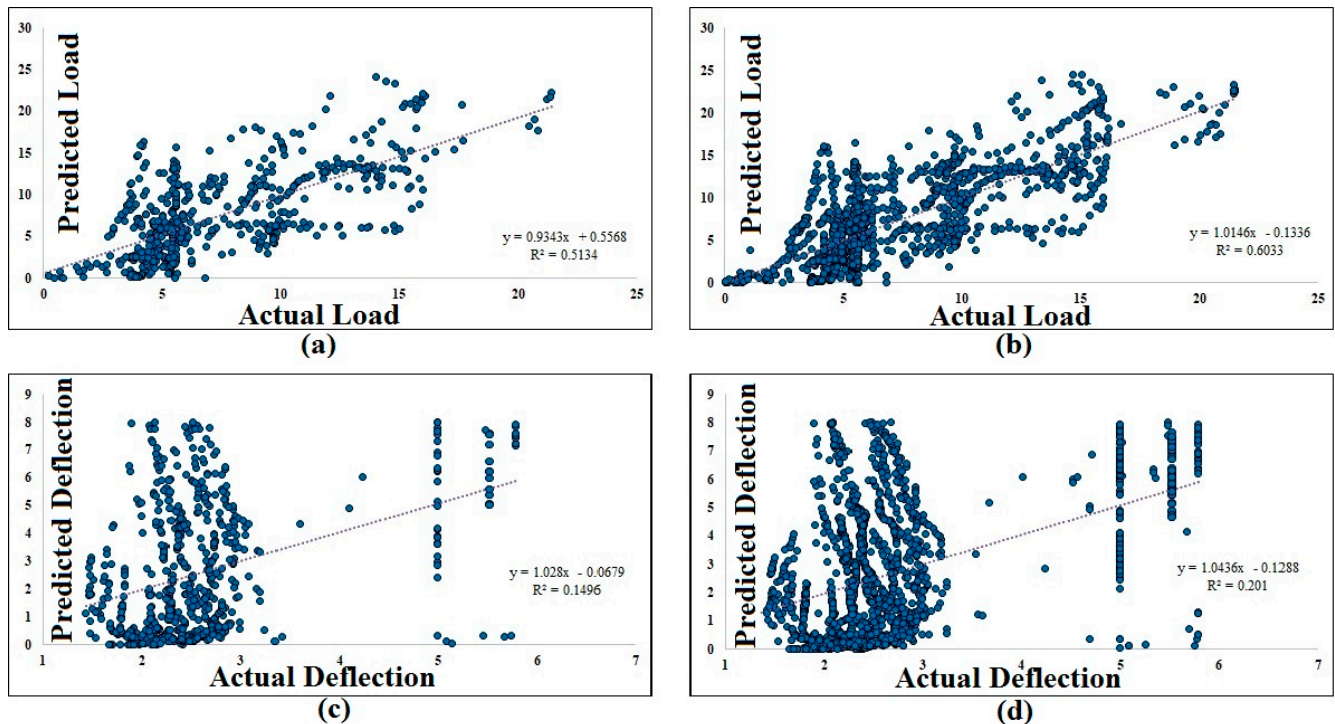
Figure 22. ANFIS-PSO prediction vs. experimental diagram for subdatabase2: (a) flexural load test phase, (b) flexural load train phase, (c) deflection test phase, (d) deflection train phase.

Table 19. Sub-database2 analytical prediction results through ANFIS-PSO.

	Test		Train	
	Flexural load prediction	RMSE	3.7334	RMSE
R <sup>2</sup>		0.4747	R <sup>2</sup>	0.5912
r		0.6890	r	0.7566
Std		3.7311	Std	3.4896
e mean		0.02019	e mean	0.0029
	Test		Train	
	Deflection prediction	RMSE	2.1251	RMSE
R <sup>2</sup>		0.1595	R <sup>2</sup>	0.1356
r		0.3993	r	0.3277
Std		2.1159	Std	2.1767
e mean		0.02150	e mean	0.0002

As before, subdatabase3 data were used to predict flexural load and deflection. Figures 23 and 24 illustrate the regression and comparative graphs of the performed analysis, respectively. Table 20 presents the results of the prediction. Due to the unsuccessful

prediction by ANFIS-PSO for FRC properties, we have employed other subdatasets for the prediction of flexural toughness of the FRC.



**Figure 23.** ANFIS-PSO prediction vs. experimental results regression for subdatabase3: (a) flexural load test phase, (b) flexural load train phase, (c) deflection test phase, (d) deflection train phase.

**Table 20.** Subdatabase3 analytical prediction results through ANFIS-PSO.

		Test		Train
Flexural load prediction	RMSE	2.1576	RMSE	2.1272
	R <sup>2</sup>	0.1496	R <sup>2</sup>	0.2010
	r	0.3785	r	0.3941
	Std	2.1594	Std	2.0926
	e mean	0.0008	e mean	0.0169
Deflection prediction		Test		Train
	RMSE	3.6708	RMSE	3.1612
	R <sup>2</sup>	0.3150	R <sup>2</sup>	0.3108
	r	0.7165	r	0.8148
	Std	3.6730	Std	3.3946
	e mean	0.0785	e mean	0.0257

In the final phase, the prediction of flexural toughness was carried out using subdatabase4 and subdatabase5. The results obtained from the analysis of subdatabase4 are depicted in Figures 25 and 26, and the corresponding quantitative metrics are presented in Table 21. Similarly, the results from subdatabase5 are illustrated in Figures 27 and 28, and the associated quantitative results are tabulated in Table 22. The predictive performance of the ANFIS-PSO algorithm was found to be remarkably accurate in estimating the flexural toughness of the samples. This success can be attributed to several factors, one of which is the presence of irregular patterns in the results of subdatabase4 and subdatabase5. The algorithm's adaptability and robustness in handling complex and irregular data patterns allowed it to effectively capture the underlying trends in the data, leading to precise predictions.

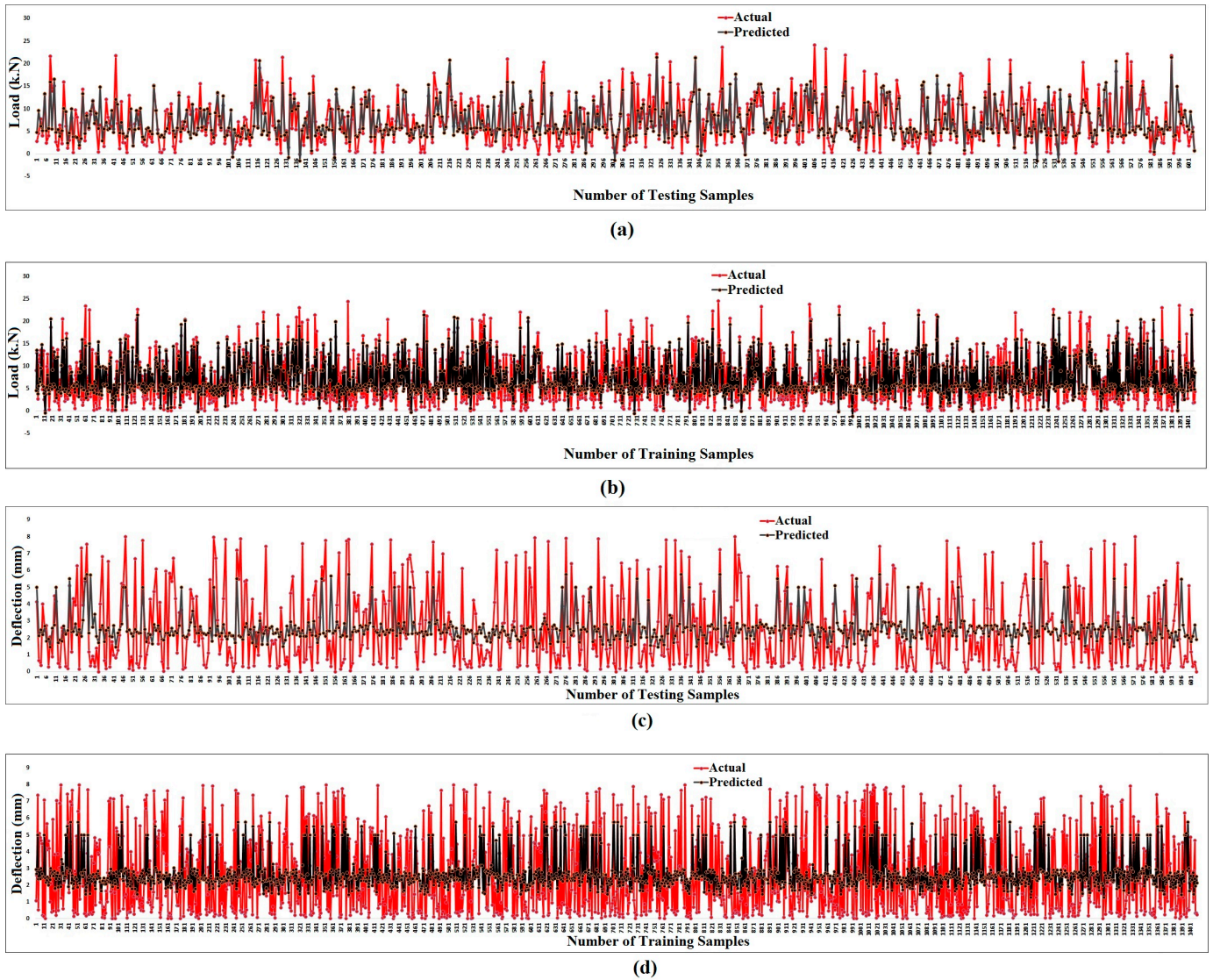


Figure 24. ANFIS-PSO prediction vs. experimental diagram for subdatabase3: (a) flexural load test phase, (b) flexural load train phase, (c) deflection test phase, (d) deflection train phase.

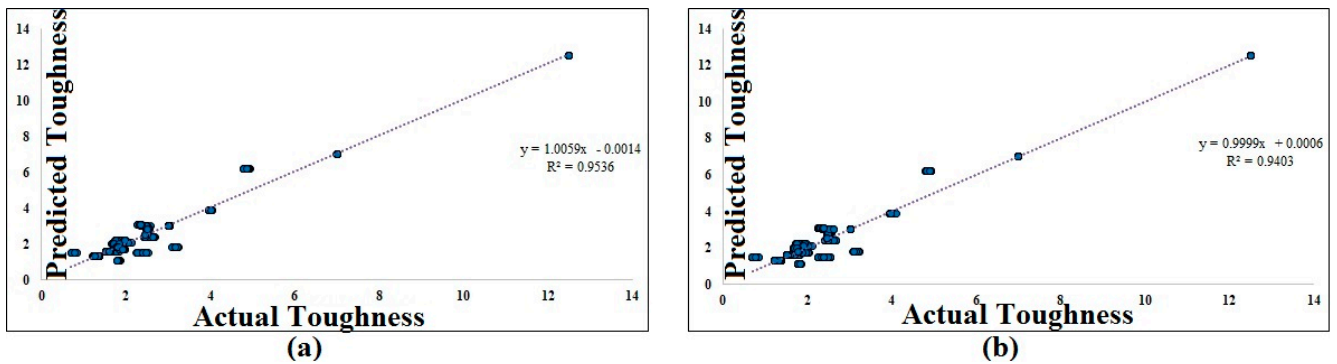


Figure 25. ANFIS-PSO prediction vs. experimental results regression for subdatabase4: (a) flexural toughness test phase, (b) flexural toughness train phase.

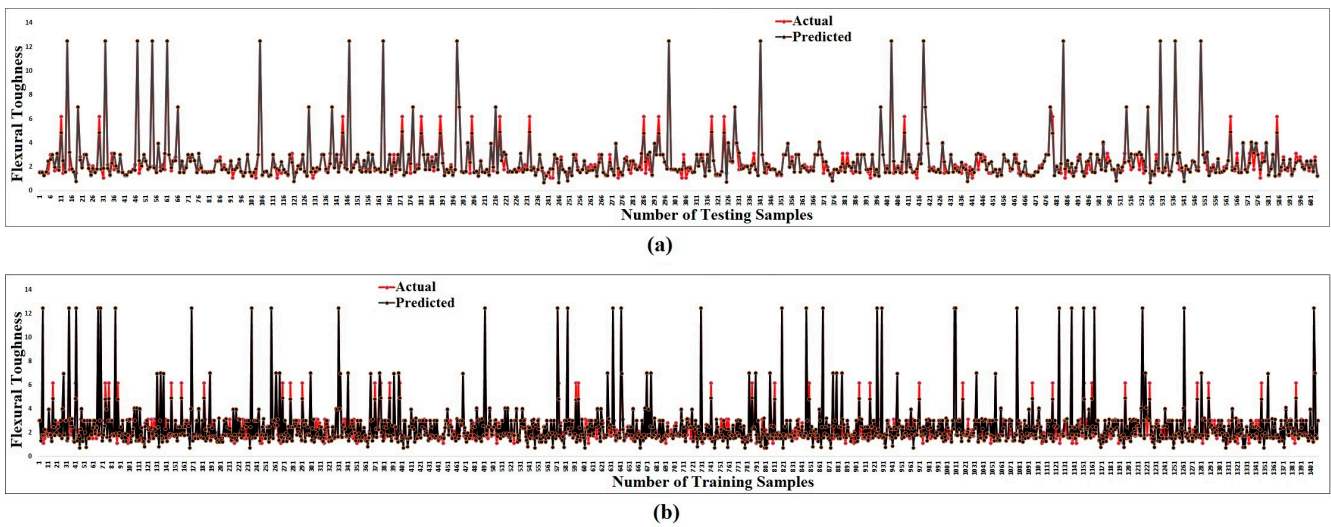


Figure 26. ANFIS-PSO prediction vs. experimental diagram for subdatabase4: (a) flexural load toughness phase, (b) flexural toughness train phase.

Table 21. Subdatabase4 analytical prediction results through ANFIS-PSO.

	Test		Train	
<b>Flexural Toughness Prediction</b>	RMSE	0.4430	RMSE	0.4588
	R <sup>2</sup>	0.9536	R <sup>2</sup>	0.9403
	r	0.9765	r	0.9710
	Std	0.4432	Std	0.4648
	e mean	0.0136	e mean	0.0003

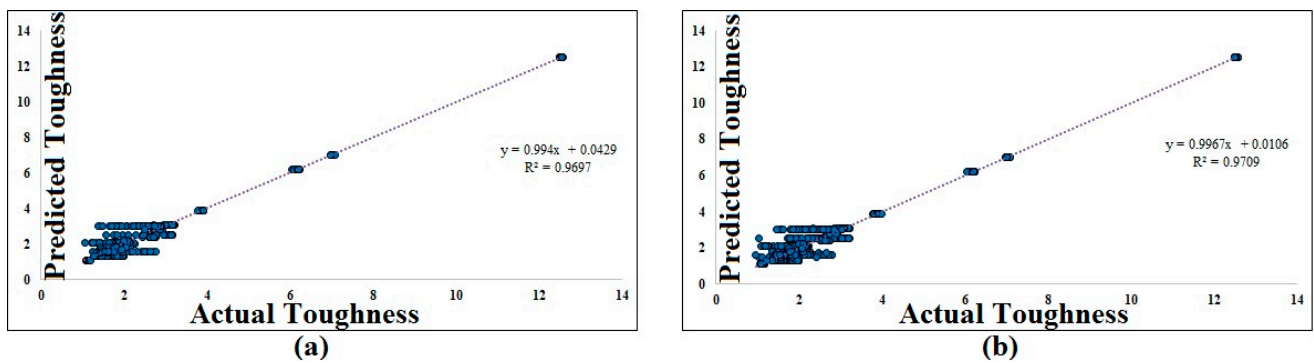
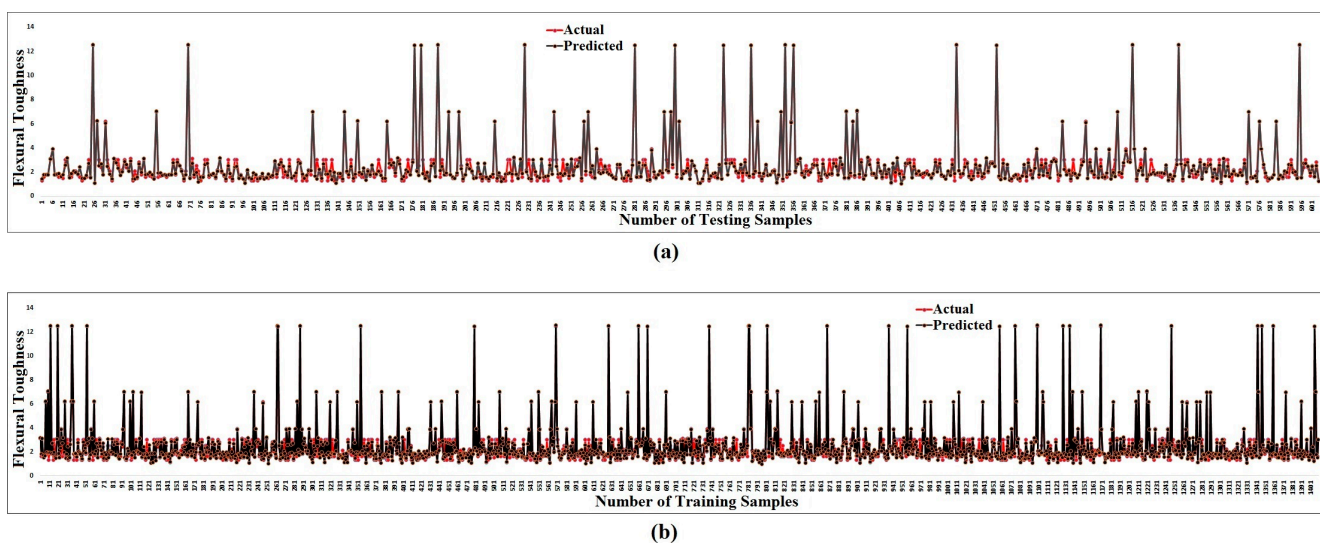


Figure 27. ANFIS-PSO prediction vs. experimental results regression for subdatabase5: (a) flexural toughness test phase, (b) flexural toughness train phase.

Table 22. Subdatabase5 analytical prediction results through ANFIS-PSO.

	Test		Train	
<b>Flexural Toughness Prediction</b>	RMSE	0.3568	RMSE	0.3453
	R <sup>2</sup>	0.9697	R <sup>2</sup>	0.9709
	r	0.9847	r	0.9808
	Std	0.3561	Std	0.3253
	e mean	0.0276	e mean	0.0023



**Figure 28.** ANFIS-PSO prediction vs. experimental diagram for subdatabase5: (a) flexural load toughness phase, (b) flexural toughness train phase.

Additionally, the presence of fiber characteristics in the samples likely played a crucial role in influencing their flexural behavior. The incorporation of fibers in fiber-reinforced concrete (FRC) is known to enhance the material's mechanical properties, including toughness. The algorithm's ability to accurately predict flexural toughness in the presence of fiber characteristics further highlights its effectiveness in capturing the impact of these material features on structural behavior. A direct comparison between Tables 21 and 22 revealed that the predictions from Table 21, which used subdatabase4, were closer to the real values. This suggests that subdatabase4, with its specific characteristics and configurations, provides more relevant and representative data for the prediction of flexural toughness. As a result, the findings conclude that the presence of fibers has a governing role in influencing the flexural behavior of fiber-reinforced concrete (FRC) specimens.

### 3.2. APG

To ensure the accuracy and reliability of the predictions, optimal values for the parameters listed in Table 15 were carefully selected. Subsequently, the data in subdatabase1 were used as inputs, and the APG algorithm was utilized to predict flexural load and deflection as the target values. The accuracy of the APG algorithm's predictions was evaluated through various quantitative metrics and graphical representations. The regression graphs and comparison graphs in Figures 29 and 30, respectively, offer visual insights into the relationship between the laboratory data and the predicted values. By plotting the predicted values against the actual data, researchers can assess the algorithm's performance in capturing the trends and patterns present in the data.

Furthermore, Table 23 presents a comprehensive summary of the analytical prediction results for this phase of the analysis. The table likely includes performance metrics such as root mean square error (RMSE), R-squared (R<sup>2</sup>), correlation coefficient (r), standard deviation (Std), and the mean error (e mean) for both flexural load and deflection predictions. These metrics are used to evaluate the accuracy, precision, and goodness of fit of the APG algorithm's predictions.

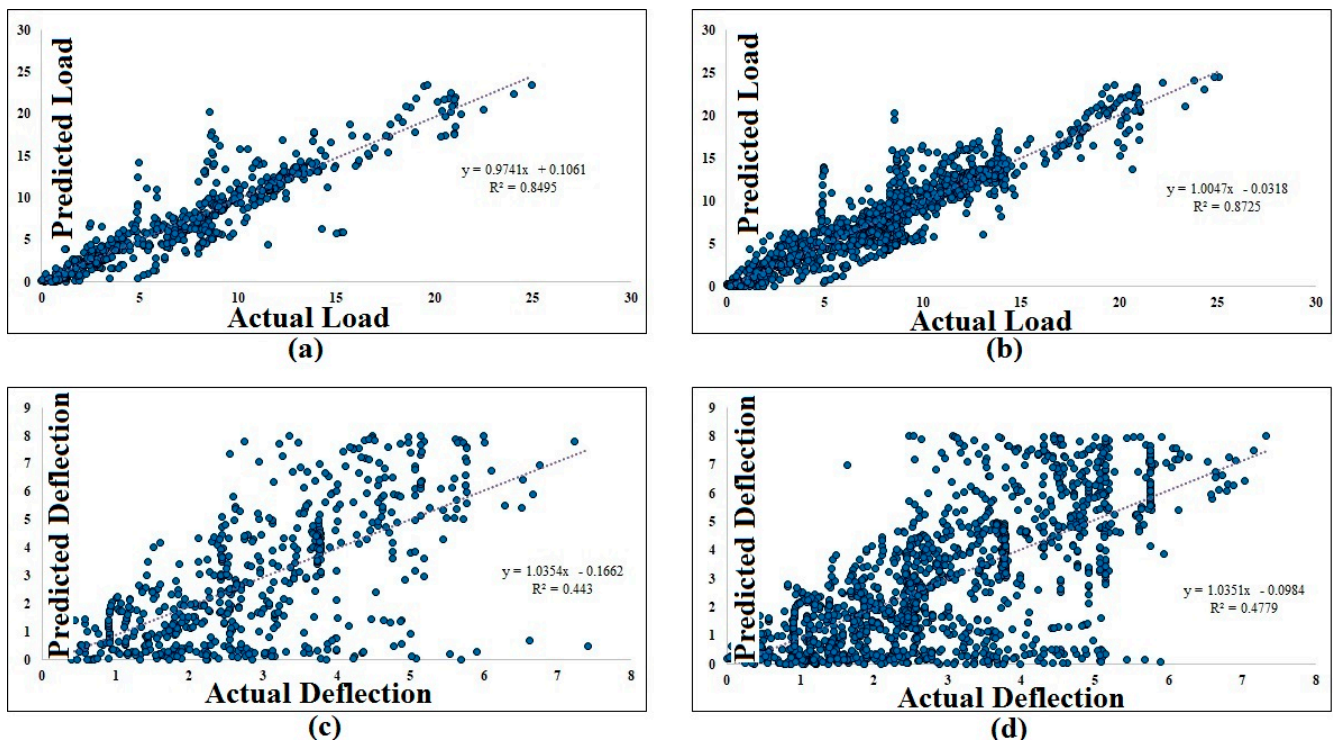


Figure 29. APG prediction vs. experimental results regression for subdatabase1: (a) flexural load test phase, (b) flexural load train phase, (c) deflection test phase, (d) deflection train phase.

Table 23. Subdatabase1 analytical prediction results through APG.

		Test		Train	
		RMSE		RMSE	
Flexural load prediction	RMSE	2.1042		1.9255	
	R <sup>2</sup>	0.8495		0.8725	
	r	0.9217		0.9342	
	Std	2.1043		1.9044	
	e mean	−0.0835		0.0037	
Deflection prediction	RMSE	1.7372		1.6368	
	R <sup>2</sup>	0.4430		0.4779	
	r	0.6656		0.7053	
	Std	1.7375		1.6888	
	e mean	−0.0633		0.0036	

For flexural load prediction in subdatabase1, the APG algorithm achieved an RMSE of 2.1042 in the test set and 1.9255 in the training set. The R-squared values were found to be 0.8495 and 0.8725 for the test and train sets, respectively. The correlation coefficient ( $r$ ) indicates a strong positive relationship between predicted and actual values, with values of 0.9217 and 0.9342 for the test and train sets, respectively. The standard deviation (Std) reflects the spread of the errors, while the mean error (e mean) represents the average error of the predictions compared to the true values.

Similarly, for deflection prediction in subdatabase1, the APG algorithm achieved an RMSE of 1.7372 in the test set and 1.6368 in the training set. The R-squared values were found to be 0.4430 and 0.4779 for the test and train sets, respectively. The correlation coefficient ( $r$ ) indicates a moderate positive relationship between predicted and actual deflection values, with values of 0.6656 and 0.7053 for the test and train sets, respectively. The standard deviation (Std) and mean error (e mean) offer additional insights into the precision and accuracy of the deflection predictions.

The obtained results from Table 23 demonstrate that the APG algorithm's predictions for flexural load are relatively accurate, as indicated by the low RMSE, high R-squared, and strong correlation coefficient values. However, the predictions for deflection show some room for improvement, with moderate R-squared values and lower correlation coefficients compared to the flexural load predictions.

In this phase of the research, subdatabase2 was utilized as the input data for the hybrid algorithm, and flexural load and deflection were predicted as the corresponding outputs. To assess the accuracy and performance of the hybrid algorithm, the predictions were compared with the actual data through regression and comparative graphs, as shown in Figures 31 and 32, respectively. Additionally, Table 24 presents a detailed summary of the analytical prediction results for subdatabase2 using the APG. The regression graph (Figure 30) visually depicts the relationship between the predicted and actual values of flexural load and deflection.

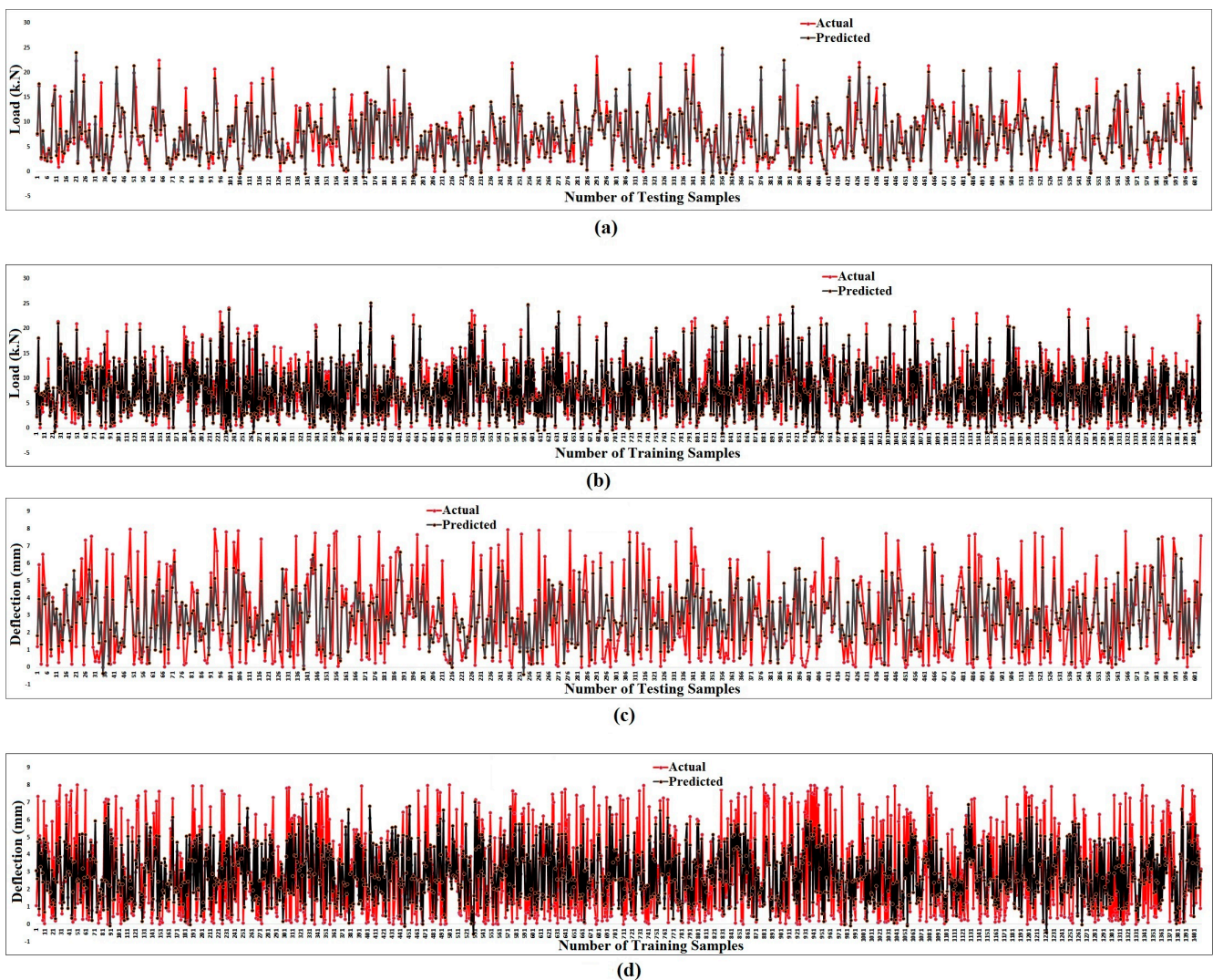


**Figure 30.** APG prediction vs. experimental diagram for subdatabase1: (a) flexural load test phase, (b) flexural load train phase, (c) deflection test phase, (d) deflection train phase.

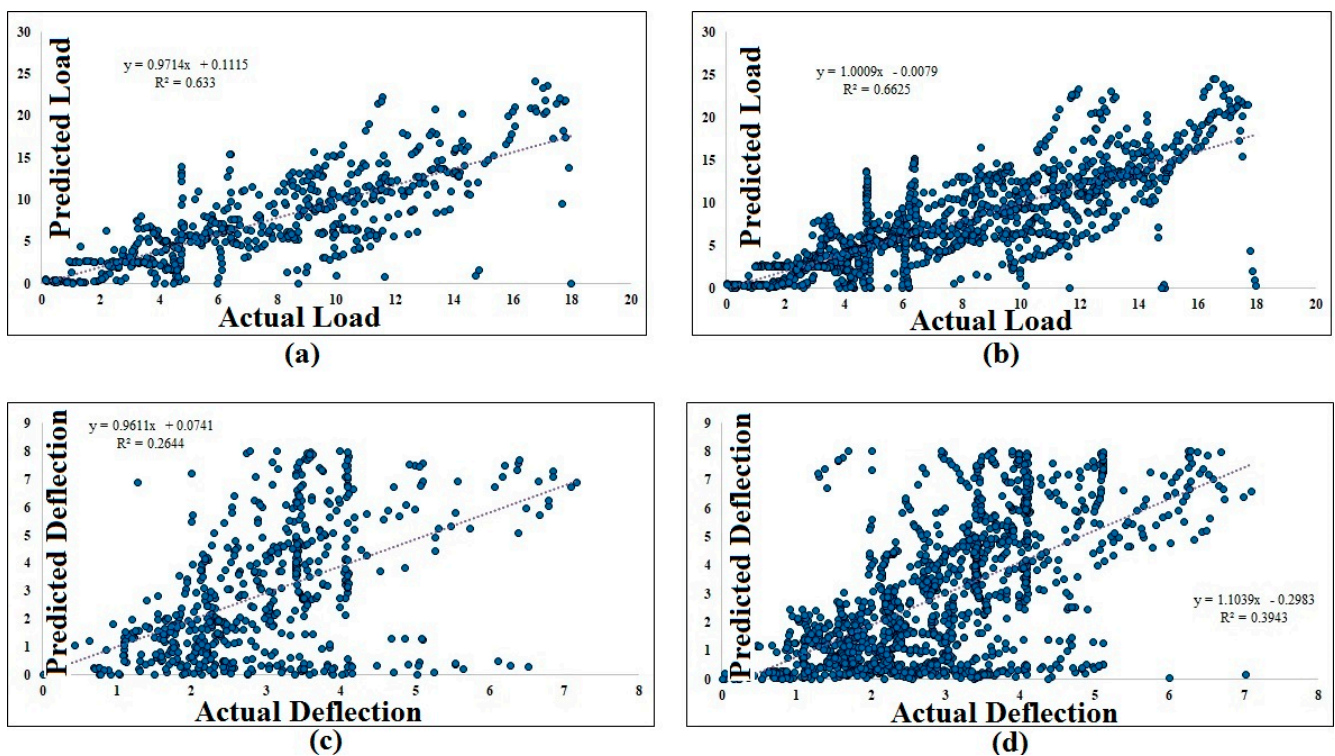


**Figure 31.** APG prediction vs. experimental results regression for subdatabase2: (a) flexural load test phase, (b) flexural load train phase, (c) deflection test phase, (d) deflection train phase.

**Table 24.** Subdatabase2 analytical prediction results through APG.

		Test		Train	
			RMSE	3.2102	RMSE
Flexural load prediction	$R^2$	0.3150	$R^2$	0.3108	
	r	0.7956	r	0.8057	
	Std	3.2110	Std	3.1290	
	e mean	−0.1069	e mean	−0.0012	
		Test		Train	
Deflection prediction	RMSE	1.9833	RMSE	1.8	
	$R^2$	0.2644	$R^2$	0.3943	
	r	0.5142	r	0.6502	
	Std	1.7375	Std	1.6888	
	e mean	−0.0412	e mean	0.0007	

Table 24 contains essential numerical properties of the analysis for subdatabase2. For the flexural load prediction, the hybrid algorithm achieved an RMSE of 3.2102 in the test set and 3.2297 in the training set. The R-squared values ( $R^2$ ) indicate the proportion of variance explained by the model, and they were found to be 0.3150 and 0.3108 for the test and train sets, respectively. The correlation coefficient (r) represents the strength of the relationship between the predicted and actual values, and values of 0.7956 and 0.8057 were obtained for the test and train sets, respectively.

Additionally, for deflection prediction in subdatabase2, the hybrid algorithm achieved an RMSE of 1.9833 in the test set and 1.8 in the training set. The R-squared values ( $R^2$ ) were found to be 0.2644 and 0.3943 for the test and train sets, respectively, indicating a moderate relationship between predicted and actual deflection values. The correlation coefficient (r) for deflection prediction was found to be 0.5142 in the test set and 0.6502 in the train set. The standard deviation (Std) and mean error (e mean) provide additional insights into the accuracy and precision of the deflection predictions.

The results presented in Table 24 indicate that the hybrid algorithm's predictions for flexural load and deflection in subdatabase2 have moderate accuracy, as indicated by the RMSE values and R-squared values, which are below the values obtained in subdatabase1. The correlation coefficients ( $r$ ) suggest that there is a significant positive relationship between predicted and actual values, but the predictive power is not as strong as observed in subdatabase1. Otherwise, subdatabase2 is not way off from subdatabase1, and this difference in accuracy could be attributed to the effect of geometrical features and fiber content on the mechanical function of FRC [59].

In this part, subdatabase3 data were utilized to predict the flexural load and deflection using the APG algorithm. The results of this prediction were evaluated and presented through regression and comparative graphs, which are depicted in Figures 33 and 34, respectively. Additionally, Table 25 offers a detailed summary of the analytical prediction results for subdatabase3 using the APG algorithm. The regression graph (Figure 33) visually showcases the relationship between the predicted and actual values of flexural load and deflection. The comparative graph (Figure 34) provides a direct comparison between the predicted and laboratory values, enabling a visual evaluation of the algorithm's performance in predicting flexural load and deflection for subdatabase3.

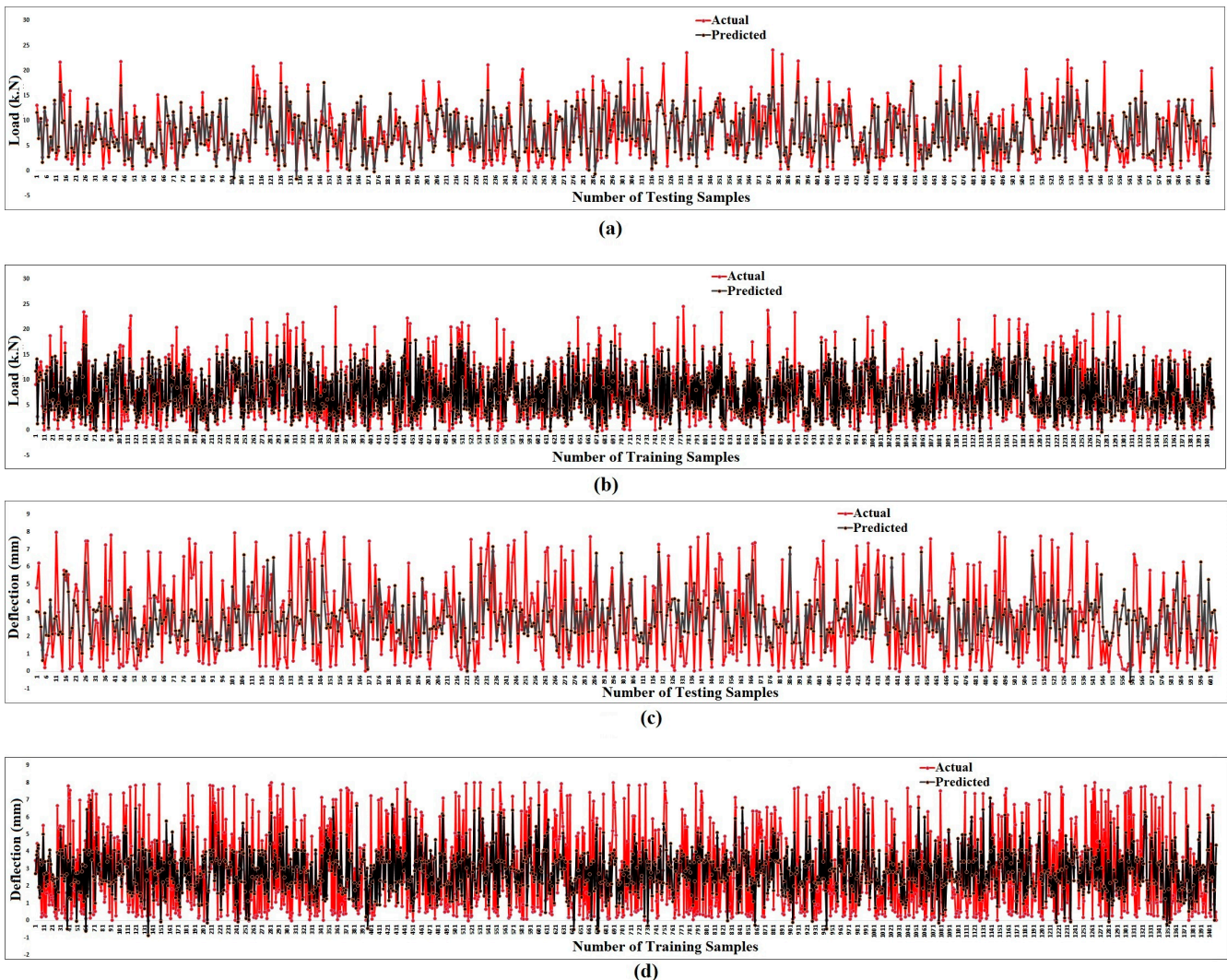


Figure 32. APG prediction vs. experimental diagram for subdatabase2: (a) flexural load test phase, (b) flexural load train phase, (c) deflection test phase, (d) deflection train phase.

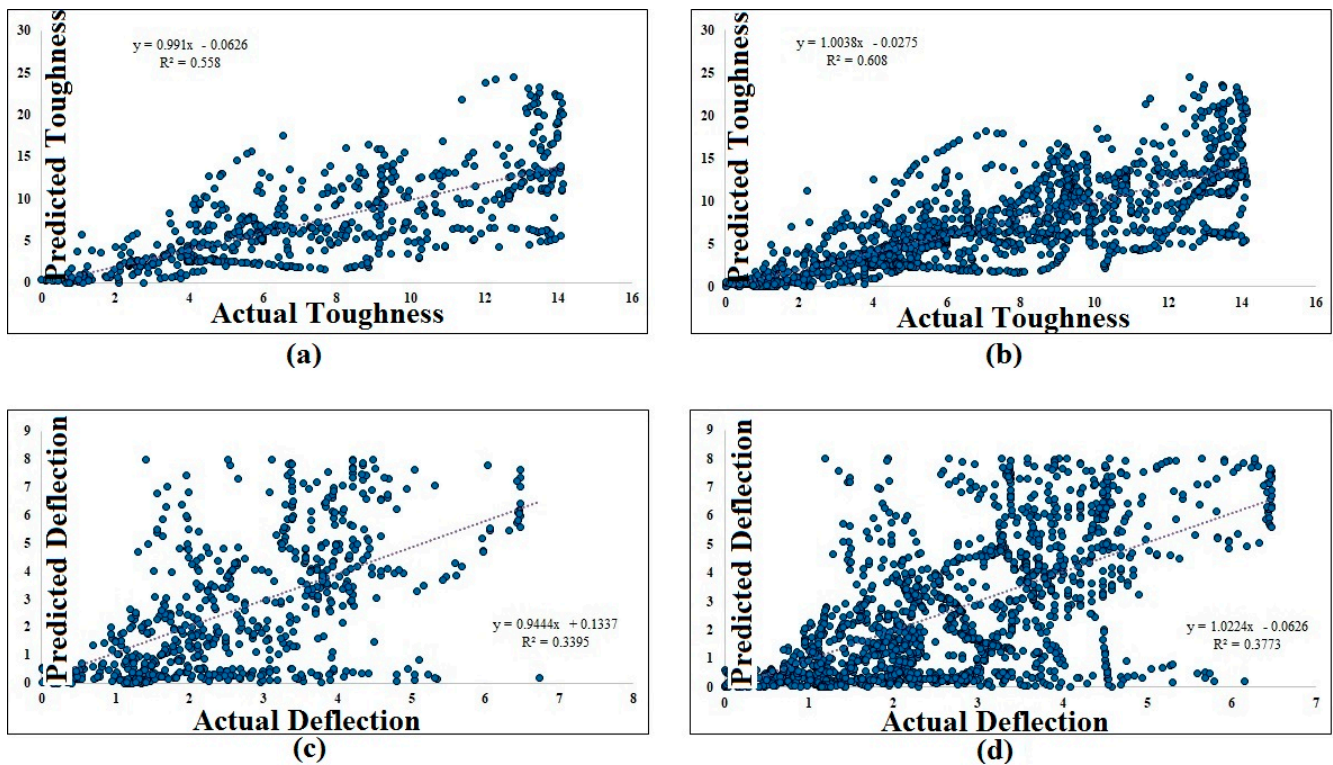


Figure 33. APG prediction vs. experimental results regression for subdatabase3: (a) flexural load test phase, (b) flexural load train phase, (c) deflection test phase, (d) deflection train phase.

Table 25. Subdatabase3 analytical prediction results through APG algorithm.

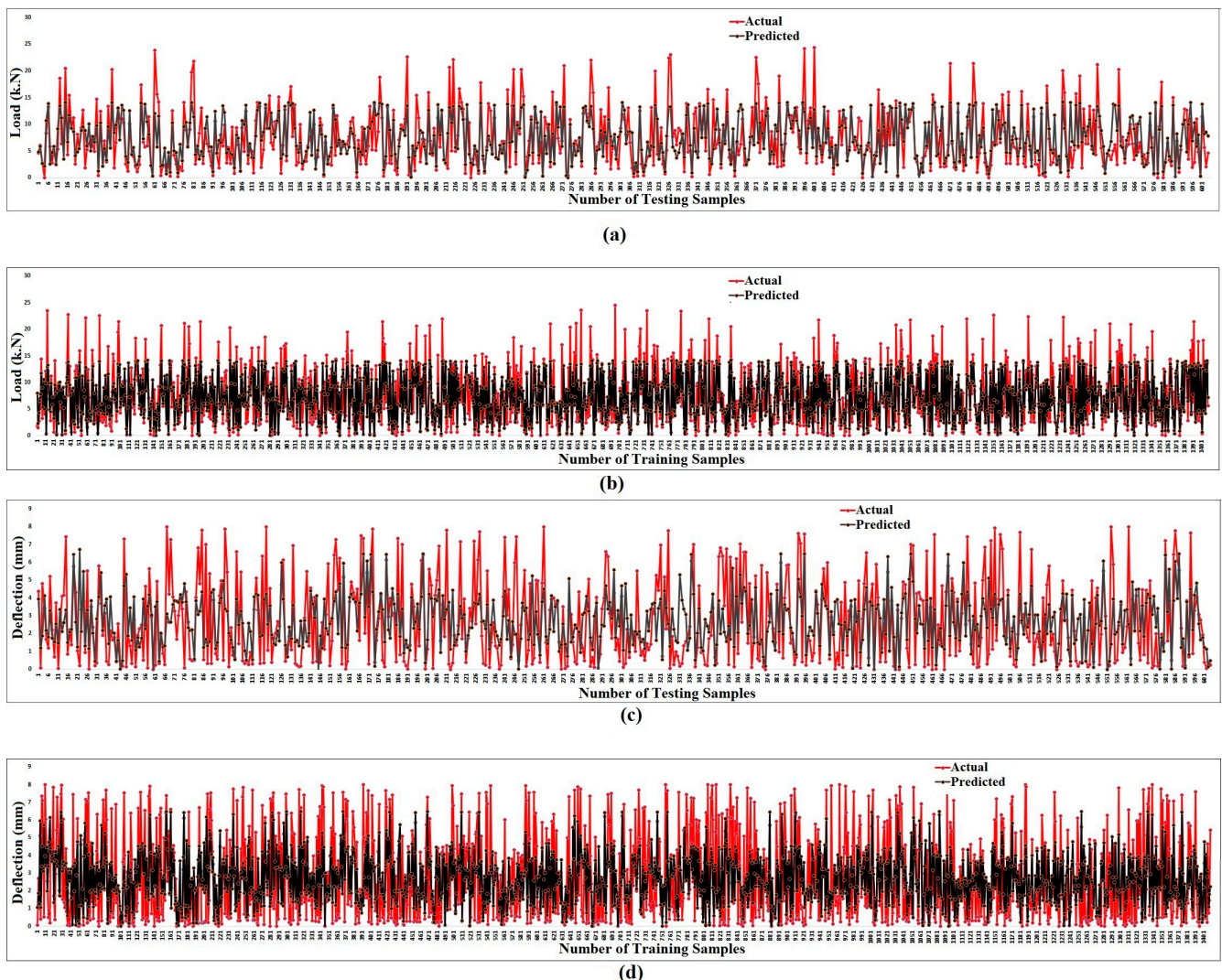
		Test		Train
Flexural load prediction	RMSE	3.5509	RMSE	3.1600
	$R^2$	0.5580	$R^2$	0.6080
	r	0.7481	r	0.7830
	Std	3.2110	Std	3.1290
	e mean	0.0760	e mean	0.0199
Deflection prediction		Test		Train
	RMSE	1.8977	RMSE	1.8748
	$R^2$	0.3395	$R^2$	0.3773
	r	0.5781	r	0.6215
	Std	1.8992	Std	1.6888
	e mean	0.0166	e mean	0.0049

Table 25 presents crucial numerical metrics derived from the prediction analysis. For flexural load prediction in subdatabase3, the APG algorithm achieved an RMSE of 3.5509 in the test set and 3.1600 in the training set. The R-squared values ( $R^2$ ) indicate the proportion of variance explained by the model, and they were found to be 0.5580 and 0.6080 for the test and train sets, respectively. The correlation coefficient (r) represents the strength of the relationship between the predicted and actual values with values of 0.7481 and 0.7830 for the test and train sets, respectively.

Similarly, for deflection prediction in subdatabase3, the APG algorithm achieved an RMSE of 1.8977 in the test set and 1.8748 in the training set. The R-squared values ( $R^2$ ) were found to be 0.3395 and 0.3773 for the test and train sets, respectively. The correlation coefficient (r) for deflection prediction was found to be 0.5781 in the test set and 0.6215 in the train set. The standard deviation (Std) and mean error (e mean) offer additional insights into the accuracy and precision of the deflection predictions.

The results presented in Table 25 indicate that the APG algorithm's predictions for flexural load and deflection in subdatabase3 demonstrate moderate accuracy. The RMSE values and R-squared values are higher than those obtained in subdatabase1 but lower than those observed in subdatabase2. The correlation coefficients ( $r$ ) suggest a positive relationship between predicted and actual values, indicating that the algorithm is capturing relevant patterns in the data. This smooth performance of the APG algorithm thoroughly confirms that the elasticity of the fibers has a significant role in the flexural behavior of FRC [33–35].

In the final step of the research, the prediction of flexural toughness involved the use of two separate subdatabases: subdatabase4 and subdatabase5. The results obtained from the analysis of subdatabase4 are illustrated in Figures 35 and 36, with a comprehensive summary of the analytical prediction outcomes presented in Table 26. Similarly, the results obtained from the analysis of subdatabase5 are shown in Figures 37 and 38 along with the associated analytical prediction metrics presented in Table 27.



**Figure 34.** APG prediction vs. experimental diagram for subdatabase3: (a) flexural load test phase, (b) flexural load train phase, (c) deflection test phase, (d) deflection train phase.

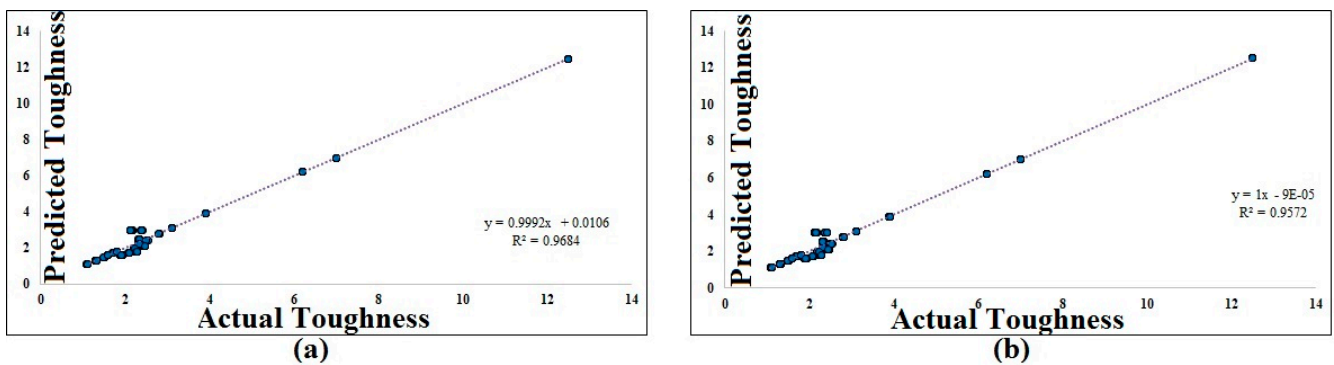


Figure 35. APG prediction vs. experimental results regression for subdatabase4: (a) flexural toughness test phase, (b) flexural toughness train phase.

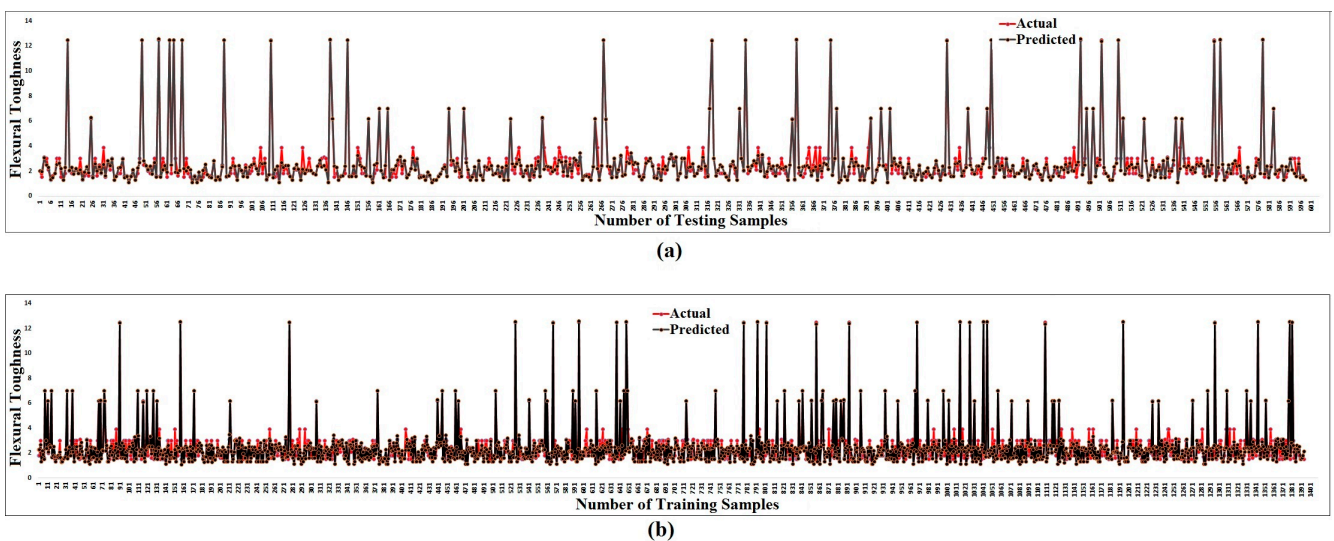


Figure 36. APG prediction vs. experimental diagram for subdatabase4: (a) flexural load toughness phase, (b) flexural toughness train phase.

Table 26. Subdatabase4 analytical prediction results through APG algorithm.

	Test		Train	
	<b>Flexural Toughness Prediction</b>	RMSE	0.3772	RMSE
	R <sup>2</sup>	0.9684	R <sup>2</sup>	0.9572
	r	0.9841	r	0.9780
	Std	0.3775	Std	0.3865
	e mean	0.0084	e mean	0.0000

Table 27. Subdatabase5 analytical prediction results through APG algorithm.

	Test		Train	
	<b>Flexural Toughness Prediction</b>	RMSE	0.3776	RMSE
	R <sup>2</sup>	0.9642	R <sup>2</sup>	0.9628
	r	0.9819	r	0.9821
	Std	0.3777	Std	0.3670
	e mean	0.0130	e mean	0.0001

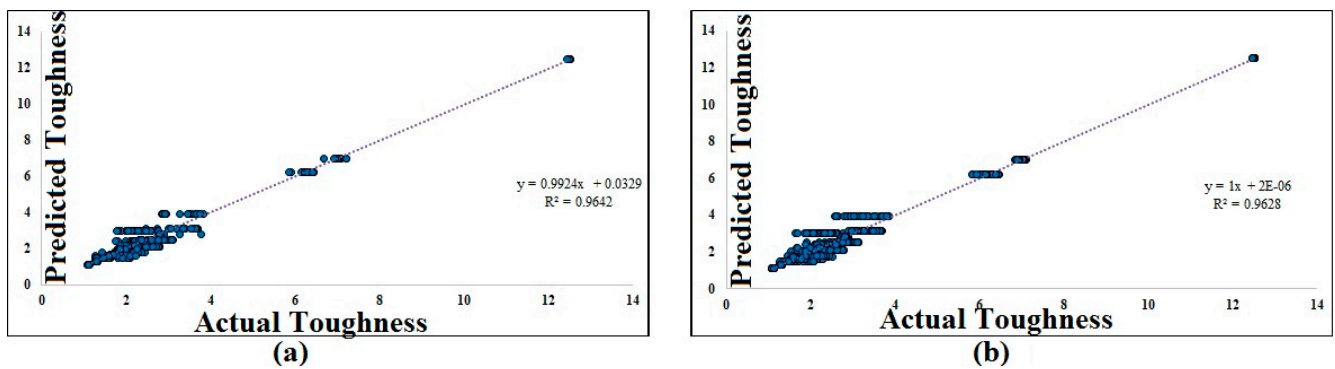


Figure 37. APG prediction vs. experimental results regression for subdatabase5: (a) flexural toughness test phase, (b) flexural toughness train phase.

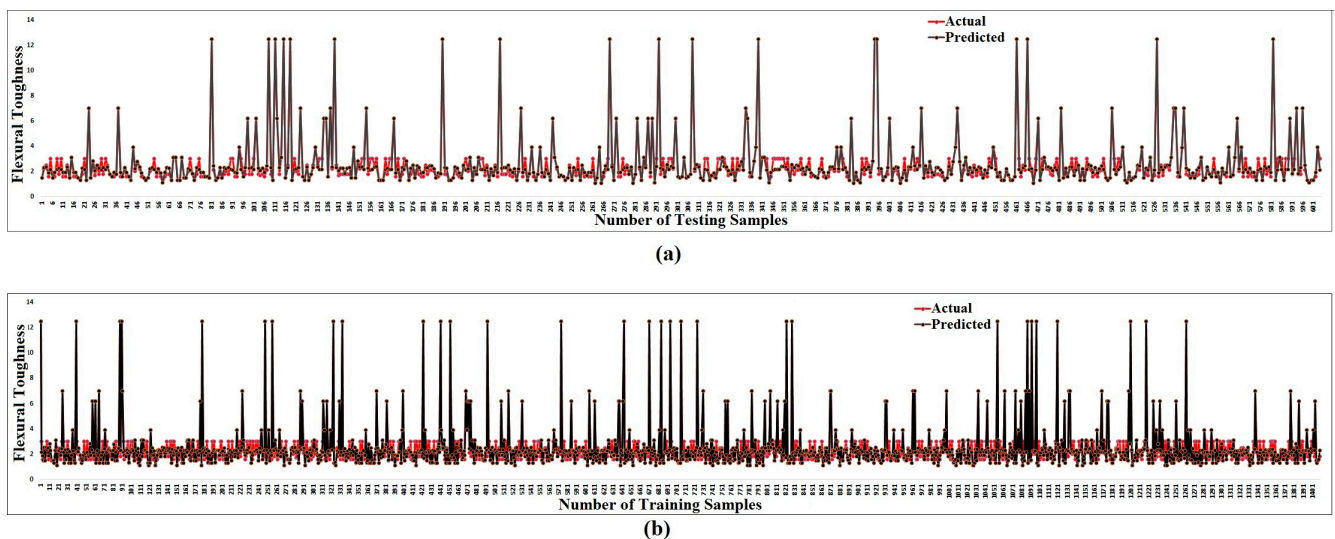


Figure 38. APG prediction vs. experimental diagram for subdatabase5: (a) flexural load toughness phase, (b) flexural toughness train phase.

Table 26 provides a detailed assessment of the APG (Artificial Pollination Algorithm) algorithm's predictive performance for flexural toughness in subdatabase4. The algorithm's predictions were evaluated using various metrics, such as the root mean square error (RMSE), R-squared ( $R^2$ ), correlation coefficient ( $r$ ), standard deviation (Std), and mean error (e mean). The RMSE values indicate the average magnitude of the errors in predicting flexural toughness for the test and train sets, respectively. The R-squared values ( $R^2$ ) indicate the proportion of variance in the data explained by the algorithm's predictions, with higher values suggesting better predictive performance. The correlation coefficients ( $r$ ) represent the strength and direction of the linear relationship between the predicted and actual flexural toughness values, while the standard deviation (Std) and mean error (e mean) offer insights into the precision and accuracy of the algorithm's predictions.

For subdatabase4, the APG algorithm demonstrated excellent predictive performance for flexural toughness, with an RMSE of 0.3772 for the test set and 0.3919 for the train set. The high R-squared values of 0.9684 and 0.9572 for the test and train sets, respectively, indicate that a significant portion of the variance in the flexural toughness data is explained by the algorithm's predictions. The correlation coefficients ( $r$ ) of 0.9841 for the test set and 0.9780 for the train set signify strong positive linear relationships between predicted and actual values. Additionally, the small standard deviation (Std) values of 0.3775 for the test set and 0.3865 for the train set, along with the mean error (e mean) values close to zero, demonstrate the algorithm's precision and accuracy in predicting flexural toughness [50].

Likewise, Table 27 presents the analytical prediction results for flexural toughness in subdatabase5 using the APG algorithm. The algorithm's predictive performance metrics are evaluated and include RMSE, R-squared (R<sup>2</sup>), correlation coefficient (r), standard deviation (Std), and mean error (e mean). The results indicate that the APG algorithm achieved an RMSE of 0.3776 for the test set and 0.3749 for the train set, showcasing consistent performance. The R-squared values (R<sup>2</sup>) of 0.9642 for the test set and 0.9628 for the train set suggest strong predictive capabilities of the algorithm. The correlation coefficients (r) of 0.9819 for the test set and 0.9821 for the train set indicate a highly positive linear relationship between predicted and actual values. Moreover, the small standard deviation (Std) values of 0.3777 for the test set and 0.3670 for the train set, along with the mean error (e mean) values close to zero, further confirm the algorithm's accuracy and precision in predicting flexural toughness in subdatabase5 [45].

The findings from Tables 26 and 27 demonstrate that the APG algorithm successfully predicts flexural toughness for both subdatabase4 and subdatabase5 with high accuracy and precision. The high R-squared values and strong correlation coefficients indicate that the algorithm captures the complex relationships between input data and flexural toughness with exceptional accuracy [55–57]. The consistently low RMSE and small standard deviation values further validate the reliability and consistency of the algorithm's predictions.

#### 4. Conclusions

In this study, the behavior of fibrous concrete under elevated temperatures was investigated using a novel design artificial intelligence algorithm called APG (ANFIS-PSO-GA hybrid algorithm). By combining ANFIS (Adaptive Neuro-Fuzzy Inference System) with population-based algorithms, including the genetic algorithm and the particle swarm optimization algorithm, the APG algorithm was developed for comprehensive evaluation. Although using AI (artificial intelligence) has facilitated modeling the behavior of FRC, lack of data and time-consuming analysis were limitations of the work. The experimental test data were divided into five subdatasets to thoroughly analyze the performance of the algorithms. Based on the achieved results, several important conclusions were drawn.

- Firstly, it was observed that fibers play a significant governing role in the flexural behavior of fiber-reinforced concrete (FRC), especially at elevated temperatures. The incorporation of fibers in concrete enhances its strain capacity, impact resistance, energy absorption, wear resistance, and tensile strength, which are crucial properties for various engineering applications.
- Among the mechanical properties of FRC, the flexural load was identified as the most influential factor. The APG algorithm successfully predicted the deflection and flexural characteristics (flexural load and flexural toughness) of FRC. Notably, flexural toughness was found to be directly related to the mechanical properties of the fibers.
- The findings highlight the importance of evaluating the fiber content and fiber elasticity to design suitable FRC samples with desired properties. The proper selection and evaluation of fibers are essential for achieving the desired mechanical performance and behavior of FRC under different conditions.
- The APG algorithm demonstrated superior performance and accuracy in estimating the flexural properties of FRC compared to the ANFIS-PSO algorithm. The successful application of the APG algorithm paves the way for further studies to predict and evaluate other properties of FRC, such as compressive strength, using the same approach. Additionally, exploring the combination of population-based heuristic algorithms with Convolutional Neural Networks presents another promising avenue for challenging and enhancing prediction results.

In conclusion, this study presents a novel and effective approach to evaluate the behavior of fibrous concrete under elevated temperatures using the APG algorithm. The results demonstrate the importance of fibers in influencing the flexural behavior of FRC and provide valuable insights for designing and optimizing FRC compositions for specific engineering applications. The successful application of the APG algorithm in predicting

flexural properties opens up new possibilities for material characterization and structural analysis in the field of civil engineering. For future research, the suggested extension of the APG algorithm to predict other properties of FRC and explore hybridization with Convolutional Neural Networks promises to further advance the understanding and application of artificial intelligence in concrete technology and structural engineering.

**Author Contributions:** Conceptualization, H.F. and A.E.R.; methodology, L.C. and H.F.; validation, M.M.; formal analysis, L.C.; investigation, M.M.; writing—original draft preparation, L.C.; writing—review and editing, H.F.; supervision, H.F.; project administration, M.M. and A.E.R.; funding acquisition, A.E.R. All authors have read and agreed to the published version of the manuscript.

**Funding:** This research was funded by the Deputyship for Research & Innovation, Ministry of Education in Saudi Arabia through the project no. (IFKSUOR3-582-1).

**Data Availability Statement:** Not applicable.

**Acknowledgments:** This work was supported by the Science and Technology Research Program of Chongqing Municipal Education Commission (Grant No. KJQN202203420).

**Conflicts of Interest:** The authors declare no conflict of interest.

## References

1. Mehrabi, P.; Shariati, M.; Kabirifar, K.; Jarrah, M.; Rasekh, H.; Trung, N.T.; Shariati, A.; Jahandari, S. Effect of pumice powder and nano-clay on the strength and permeability of fiber-reinforced pervious concrete incorporating recycled concrete aggregate. *Constr. Build. Mater.* **2021**, *287*, 122652. [[CrossRef](#)]
2. Han, S.; Zhu, Z.; Mortazavi, M.; El-Sherbeeney, A.M.; Mehrabi, P. Analytical Assessment of the Structural Behavior of a Specific Composite Floor System at Elevated Temperatures Using a Newly Developed Hybrid Intelligence Method. *Buildings* **2023**, *13*, 799. [[CrossRef](#)]
3. Liu, Y.; Li, J.; Lin, G. Seismic performance of advanced three-dimensional base-isolated nuclear structures in complex-layered sites. *Eng. Struct.* **2023**, *289*, 116247. [[CrossRef](#)]
4. Wang, W.; Li, D.-Q.; Tang, X.-S.; Du, W. Seismic fragility and demand hazard analyses for earth slopes incorporating soil property variability. *Soil Dyn. Earthq. Eng.* **2023**, *173*, 108088. [[CrossRef](#)]
5. Jin, M.; Ma, Y.; Li, W.; Huang, J.; Yan, Y.; Zeng, H.; Lu, C.; Liu, J. Multi-scale investigation on composition-structure of C-(A)-SH with different Al/Si ratios under attack of decalcification action. *Cem. Concr. Res.* **2023**, *172*, 107251. [[CrossRef](#)]
6. Zhang, W.; Kang, S.; Huang, Y.; Liu, X. Behavior of reinforced concrete beams without stirrups and strengthened with basalt fiber-reinforced polymer sheets. *J. Compos. Constr.* **2023**, *27*, 04023007.
7. Wang, H.; Zhang, X.; Jiang, S. A laboratory and field universal estimation method for tire–pavement interaction noise (TPIN) based on 3D image technology. *Sustainability* **2022**, *14*, 12066. [[CrossRef](#)]
8. Wang, H.; Zhang, X.; Wang, M. Rapid texture depth detection method considering pavement deformation calibration. *Measurement* **2023**, *217*, 113024. [[CrossRef](#)]
9. Yang, H.; Li, Z.; Jie, T.; Zhang, Z. Effects of joints on the cutting behavior of disc cutter running on the jointed rock mass. *Tunn. Undergr. Space Technol.* **2018**, *81*, 112–120. [[CrossRef](#)]
10. Shi, T.; Liu, Y.; Hu, Z.; Cen, M.; Zeng, C.; Xu, J.; Zhao, Z. Deformation performance and fracture toughness of carbon nanofiber-modified cement-based materials. *ACI Mater. J.* **2022**, *119*, 119–128.
11. Li, J.; Chen, M.; Li, Z. Improved soil–structure interaction model considering time-lag effect. *Comput. Geotech.* **2022**, *148*, 104835. [[CrossRef](#)]
12. Hong, Y.; Yao, M.; Wang, L. A multi-axial bounding surface py model with application in analyzing pile responses under multi-directional lateral cycling. *Comput. Geotech.* **2023**, *157*, 105301. [[CrossRef](#)]
13. Alsaif, A.; Alharbi, Y.R. Strength, durability and shrinkage behaviours of steel fiber reinforced rubberized concrete. *Constr. Build. Mater.* **2022**, *345*, 128295. [[CrossRef](#)]
14. Behfarnia, K.; Behravan, A. Application of high performance polypropylene fibers in concrete lining of water tunnels. *Mater. Des.* **2014**, *55*, 274–279. [[CrossRef](#)]
15. Deng, Z.; Li, J. Mechanical behaviors of concrete combined with steel and synthetic macro-fibers. *Comput. Concr. Int. J.* **2007**, *4*, 207–220. [[CrossRef](#)]
16. Snoeck, D.; De Belie, N. From straw in bricks to modern use of microfibers in cementitious composites for improved autogenous healing—A review. *Constr. Build. Mater.* **2015**, *95*, 774–787. [[CrossRef](#)]
17. Arnon Bentur, S.M. *Fibre Reinforced Cementitious Composites*, 2nd ed.; CRC Press: Boca Raton, FL, USA, 2007; p. 624.
18. Zollo, R.F. Fiber-reinforced concrete: An overview after 30 years of development. *Cem. Concr. Compos.* **1997**, *19*, 107–122. [[CrossRef](#)]
19. Morgan, D.R.; Jolin, M. *Shotcrete: Materials, Performance and Use*; CRC Press: Boca Raton, FL, USA, 2022; Volume 22.

20. Xu, Y.; Chung, D. Reducing the drying shrinkage of cement paste by admixture surface treatments. *Cem. Concr. Res.* **2000**, *30*, 241–245. [[CrossRef](#)]
21. Shariati, M.; Mafipour, M.S.; Mehrabi, P.; Zandi, Y.; Dehghani, D.; Bahadori, A.; Shariati, A.; Trung, N.T.; Salih, M.; Poi-Ngian, S. Application of Extreme Learning Machine (ELM) and Genetic Programming (GP) to design steel-concrete composite floor systems at elevated temperatures. *Steel Compos. Struct* **2019**, *33*, 319–332.
22. Fang, B.; Hu, Z.; Shi, T.; Liu, Y.; Wang, X.; Yang, D.; Zhu, K.; Zhao, X.; Zhao, Z. Research progress on the properties and applications of magnesium phosphate cement. *Ceram. Int.* **2022**, *49*, 4001–4016.
23. Liu, C.; Cui, J.; Zhang, Z.; Liu, H.; Huang, X.; Zhang, C. The role of TBM asymmetric tail-grouting on surface settlement in coarse-grained soils of urban area: Field tests and FEA modelling. *Tunn. Undergr. Space Technol.* **2021**, *111*, 103857.
24. Lau, A.; Anson, M. Effect of high temperatures on high performance steel fibre reinforced concrete. *Cem. Concr. Res.* **2006**, *36*, 1698–1707. [[CrossRef](#)]
25. Moghadam, M.A.; Izadifard, R. Evaluation of shear strength of plain and steel fibrous concrete at high temperatures. *Constr. Build. Mater.* **2019**, *215*, 207–216. [[CrossRef](#)]
26. Uysal, M.; Tanyildizi, H. Estimation of compressive strength of self compacting concrete containing polypropylene fiber and mineral additives exposed to high temperature using artificial neural network. *Constr. Build. Mater.* **2012**, *27*, 404–414. [[CrossRef](#)]
27. Khoury, G. Polypropylene fibres in heated concrete. Part 2: Pressure relief mechanisms and modelling criteria. *Mag. Concr. Res.* **2008**, *60*, 189–204. [[CrossRef](#)]
28. Pliya, P.; Beaucour, A.; Noumowé, A. Contribution of cocktail of polypropylene and steel fibres in improving the behaviour of high strength concrete subjected to high temperature. *Constr. Build. Mater.* **2011**, *25*, 1926–1934. [[CrossRef](#)]
29. Sukontasukkul, P.; Pomchiengpin, W.; Songpiriyakij, S. Post-crack (or post-peak) flexural response and toughness of fiber reinforced concrete after exposure to high temperature. *Constr. Build. Mater.* **2010**, *24*, 1967–1974. [[CrossRef](#)]
30. Çavdar, A. The effects of high temperature on mechanical properties of cementitious composites reinforced with polymeric fibers. *Compos. Part B Eng.* **2013**, *45*, 78–88. [[CrossRef](#)]
31. Huang, H.; Yao, Y.; Liang, C.; Ye, Y. Experimental study on cyclic performance of steel-hollow core partially encased composite spliced frame beam. *Soil Dyn. Earthq. Eng.* **2022**, *163*, 107499. [[CrossRef](#)]
32. Abedini, M.; Zhang, C. Residual capacity assessment of post-damaged RC columns exposed to high strain rate loading. *Steel Compos. Struct.* **2022**, *45*, 389–408.
33. Yang, H.; Zeng, Y.; Lan, Y.; Zhou, X. Analysis of the excavation damaged zone around a tunnel accounting for geostress and unloading. *Int. J. Rock Mech. Min. Sci.* **2014**, *69*, 59–66. [[CrossRef](#)]
34. Hu, D.; Sun, H.; Mehrabi, P.; Ali, Y.A.; Al-Razgan, M. Application of artificial intelligence technique in optimization and prediction of the stability of the walls against wind loads in building design. *Mech. Adv. Mater. Struct.* **2023**, 1–18. [[CrossRef](#)]
35. Far, C.; Far, H. Improving energy efficiency of existing residential buildings using effective thermal retrofit of building envelope. *Indoor Built Environ.* **2019**, *28*, 744–760. [[CrossRef](#)]
36. Xia, Y.; Shi, M.; Zhang, C.; Wang, C.; Sang, X.; Liu, R.; Zhao, P.; An, G.; Fang, H. Analysis of flexural failure mechanism of ultraviolet cured-in-place-pipe materials for buried pipelines rehabilitation based on curing temperature monitoring. *Eng. Fail. Anal.* **2022**, *142*, 106763. [[CrossRef](#)]
37. Huang, H.; Li, M.; Yuan, Y.; Bai, H. Theoretical analysis on the lateral drift of precast concrete frame with replaceable artificial controllable plastic hinges. *J. Build. Eng.* **2022**, *62*, 105386. [[CrossRef](#)]
38. Liu, B.; Yang, H.; Karekal, S. Effect of water content on argillization of mudstone during the tunnelling process. *Rock Mech. Rock Eng.* **2020**, *53*, 799–813. [[CrossRef](#)]
39. Huang, Y.; Zhang, W.; Liu, X. Assessment of diagonal macrocrack-induced debonding mechanisms in FRP-strengthened RC beams. *J. Compos. Constr.* **2022**, *26*, 04022056. [[CrossRef](#)]
40. Zhang, W.; Kang, S.; Liu, X.; Lin, B.; Huang, Y. Experimental study of a composite beam externally bonded with a carbon fiber-reinforced plastic plate. *J. Build. Eng.* **2023**, *71*, 106522. [[CrossRef](#)]
41. Zhang, Z.; Li, W.; Yang, J. Analysis of stochastic process to model safety risk in construction industry. *J. Civ. Eng. Manag.* **2021**, *27*, 87–99. [[CrossRef](#)]
42. Xu, L.; Cai, M.; Dong, S.; Yin, S.; Xiao, T.; Dai, Z.; Wang, Y.; Soltanian, M.R. An upscaling approach to predict mine water inflow from roof sandstone aquifers. *J. Hydrol.* **2022**, *612*, 128314. [[CrossRef](#)]
43. Chen, L.; Yang, H.; Song, K.; Huang, W.; Ren, X.; Xu, H. Failure mechanisms and characteristics of the Zhongbao landslide at Liujing Village, Wulong, China. *Landslides* **2021**, *18*, 1445–1457. [[CrossRef](#)]
44. Li, S.; Liu, Z. Scheduling uniform machines with restricted assignment. *Math. Biosci. Eng.* **2022**, *19*, 9697–9708. [[CrossRef](#)] [[PubMed](#)]
45. Shen, Y.; Ding, N.; Zheng, H.-T.; Li, Y.; Yang, M. Modeling relation paths for knowledge graph completion. *IEEE Trans. Knowl. Data Eng.* **2020**, *33*, 3607–3617. [[CrossRef](#)]
46. Yang, H.; Chen, C.; Ni, J.; Karekal, S. A hyperspectral evaluation approach for quantifying salt-induced weathering of sandstone. *Sci. Total Environ.* **2023**, *885*, 163886. [[CrossRef](#)] [[PubMed](#)]
47. Yang, H.; Wang, Z.; Song, K. A new hybrid grey wolf optimizer-feature weighted-multiple kernel-support vector regression technique to predict TBM performance. *Eng. Comput.* **2022**, *38*, 2469–2485.

48. Yang, H.; Song, K.; Zhou, J. Automated recognition model of geomechanical information based on operational data of tunneling boring machines. *Rock Mech. Rock Eng.* **2022**, *55*, 1499–1516. [[CrossRef](#)]
49. Han, S.; Zheng, D.; Mehdizadeh, B.; Nasr, E.A.; Khandaker, M.U.; Salman, M.; Mehrabi, P. Sustainable Design of Self-Consolidating Green Concrete with Partial Replacements for Cement through Neural-Network and Fuzzy Technique. *Sustainability* **2023**, *15*, 4752. [[CrossRef](#)]
50. Mehrabi, P.; Honarbari, S.; Rafiei, S.; Jahandari, S.; Alizadeh Bidgoli, M. Seismic response prediction of FRC rectangular columns using intelligent fuzzy-based hybrid metaheuristic techniques. *J. Ambient Intell. Humaniz. Comput.* **2021**, *12*, 10105–10123. [[CrossRef](#)]
51. Taheri, E.; Mehrabi, P.; Rafiei, S.; Samali, B. Numerical evaluation of the upright columns with partial reinforcement along with the utilisation of neural networks with combining feature-selection method to predict the load and displacement. *Appl. Sci.* **2021**, *11*, 11056. [[CrossRef](#)]
52. Wang, M.; Yang, X.; Wang, W. Establishing a 3D aggregates database from X-ray CT scans of bulk concrete. *Constr. Build. Mater.* **2022**, *315*, 125740. [[CrossRef](#)]
53. Wu, J.; Yang, Y.; Mehrabi, P.; Nasr, E.A. Efficient machine-learning algorithm applied to predict the transient shock reaction of the elastic structure partially rested on the viscoelastic substrate. *Mech. Adv. Mater. Struct.* **2023**, 1–25. [[CrossRef](#)]
54. Feng, Y.; Mohammadi, M.; Wang, L.; Rashidi, M.; Mehrabi, P. Application of artificial intelligence to evaluate the fresh properties of self-consolidating concrete. *Materials* **2021**, *14*, 4885. [[CrossRef](#)] [[PubMed](#)]
55. Han, Y.; Shao, S.; Fang, B.; Shi, T.; Zhang, B.; Wang, X.; Zhao, X. Chloride ion penetration resistance of matrix and interfacial transition zone of multi-walled carbon nanotube-reinforced concrete. *J. Build. Eng.* **2023**, *72*, 106587. [[CrossRef](#)]
56. Wu, M.; Ba, Z.; Liang, J. A procedure for 3D simulation of seismic wave propagation considering source-path-site effects: Theory, verification and application. *Earthq. Eng. Struct. Dyn.* **2022**, *51*, 2925–2955. [[CrossRef](#)]
57. Shariati, M.; Mafipour, M.S.; Mehrabi, P.; Shariati, A.; Toghroli, A.; Trung, N.T.; Salih, M.N. A novel approach to predict shear strength of tilted angle connectors using artificial intelligence techniques. *Eng. Comput.* **2021**, *37*, 2089–2109. [[CrossRef](#)]
58. Dang, P.; Cui, J.; Liu, Q.; Li, Y. Influence of source uncertainty on stochastic ground motion simulation: A case study of the 2022 Mw 6.6 Luding, China, earthquake. *Stoch. Environ. Res. Risk Assess.* **2023**, *37*, 2943–2960. [[CrossRef](#)]
59. Zhu, H.; Xue, M.; Wang, Y.; Yuan, G.; Li, X. Fast visual tracking with siamese oriented region proposal network. *IEEE Signal Process. Lett.* **2022**, *29*, 1437–1441. [[CrossRef](#)]
60. Li, R.; Zhang, H.; Chen, Z.; Yu, N.; Kong, W.; Li, T.; Wang, E.; Wu, X.; Liu, Y. Denoising method of ground-penetrating radar signal based on independent component analysis with multifractal spectrum. *Measurement* **2022**, *192*, 110886.
61. Walia, N.; Singh, H.; Sharma, A. ANFIS: Adaptive neuro-fuzzy inference system—A survey. *Int. J. Comput. Appl.* **2015**, 123.
62. Liu, C.; Peng, Z.; Cui, J.; Huang, X.; Li, Y.; Chen, W. Development of crack and damage in shield tunnel lining under seismic loading: Refined 3D finite element modeling and analyses. *Thin-Walled Struct.* **2023**, *185*, 110647.
63. Sari, P.A.; Suhatri, M.; Osman, N.; Mu'azu, M.; Katebi, J.; Abavisani, A.; Ghaffari, N.; Chahnasir, E.S.; Wakil, K.; Khorami, M. Developing a hybrid adoptive neuro-fuzzy inference system in predicting safety of factors of slopes subjected to surface eco-protection techniques. *Eng. Comput.* **2020**, *36*, 1347–1354. [[CrossRef](#)]
64. Wang, S.; Hu, X.; Sun, J.; Liu, J. Hyperspectral anomaly detection using ensemble and robust collaborative representation. *Inf. Sci.* **2023**, *624*, 748–760. [[CrossRef](#)]
65. Eberhart, R.; Kennedy, J. Particle swarm optimization. In Proceedings of the IEEE International Conference on Neural Networks, Perth, Australia, 27 November–1 December 1995; pp. 1942–1948.
66. Shariati, M.; Mafipour, M.S.; Mehrabi, P.; Bahadori, A.; Zandi, Y.; Salih, M.N.; Nguyen, H.; Dou, J.; Song, X.; Poi-Ngian, S. Application of a hybrid artificial neural network-particle swarm optimization (ANN-PSO) model in behavior prediction of channel shear connectors embedded in normal and high-strength concrete. *Appl. Sci.* **2019**, *9*, 5534. [[CrossRef](#)]
67. Liu, J.; Mohammadi, M.; Zhan, Y.; Zheng, P.; Rashidi, M.; Mehrabi, P. Utilizing artificial intelligence to predict the superplasticizer demand of self-consolidating concrete incorporating pumice, slag, and fly ash powders. *Materials* **2021**, *14*, 6792. [[CrossRef](#)] [[PubMed](#)]

**Disclaimer/Publisher's Note:** The statements, opinions and data contained in all publications are solely those of the individual author(s) and contributor(s) and not of MDPI and/or the editor(s). MDPI and/or the editor(s) disclaim responsibility for any injury to people or property resulting from any ideas, methods, instructions or products referred to in the content.